Age-related Changes in Diffuse Optical Tomography Sensitivity to the Cortex in Infancy

Xiaoxue Fu [a], John E. Richards [a]

[a] Department of Psychology, University of South Carolina, United States

Corresponding author:

Xiaoxue Fu

Email address: xiaoxuef@mailbox.sc.edu

Highlights

- Localization for diffuse optical tomography (DOT) requires age-appropriate head models.
- We constructed DOT head models for infants (2 weeks to 24 months), children and adults.
- The scalp-to-cortex distance and cranio-cerebral mapping differed among age groups.
- DOT sensitivity profiles differed by age and changed across channel separations.
- The findings inform channel placement and DOT image reconstruction.

Abstract

Diffuse optical tomography (DOT) uses near-infrared light spectroscopy (NIRS) to measure changes in cerebral hemoglobin concentration. Anatomical interpretations of the location that generates the hemodynamic signal requires accurate descriptions of the cranio-cerebral relations and DOT sensitivity to the underlying cortical structures. Such information is limited for pediatric populations because they undergo rapid head and brain development. The present study used spatial scalp projection and photon propagation simulation methods to examine scalp-to-cortex distance, scalp-location-to-ROI mapping, and DOT sensitivity profiles in realistic head models based on MRIs. We investigated age-related differences in these measures among infants ranging from 2 weeks to 24 months with narrow age bins, children (4 and 12 years) and adults (20 to 24 years). There were age-group differences in the scalp-to-cortex distances in infancy. The developmental increase was magnified in children and adults. There were systematic age-related differences in the probabilistic mappings between scalp locations and cortical ROIs. The DOT sensitivity profiles displayed decreased fluence strength with increased penetration depth across groups. There were age-related differences in the DOT sensitivity profiles across a wide range of source-detector channel separations. Our findings have important implications in the design of sensor placement and DOT image reconstruction in NIRS and fNIRS research. Age-appropriate realistic head models should be used to provide anatomical guidance for standalone DOT data in infants.

Keywords:

Diffuse optical tomography, near-infrared light spectroscopy, Monte Carlo simulation, infant, development, head models

Introduction

Diffuse optical tomography (DOT) uses near-infrared light spectroscopy (NIRS) to measure changes in cerebral hemoglobin concentration (Huppert, Franceschini, & Boas, 2009). DOT does not provide anatomical information about the location of the hemodynamic signal. One solution for providing anatomical guidance is to co-register the positions of the recording sensors on the scalp (i.e. optodes) with structural MRIs of the head and brain. Spatial scalp projection can then be implemented to interrogate the brain region(s) underlying the scalp locations (Tsuzuki & Dan, 2014). A second approach is to generate a forward model of DOT sensitivity using photon propagation simulations (Boas, Culver, Stott, & Dunn, 2002). We broadly conceptualize DOT sensitivity as the extent to which the DOT instrument can detect changes in cortical activities in a given region that it is sampling. The forward model can then guide DOT image reconstruction to recover the brain locations of hemoglobin concentration changes (Cooper et al., 2012; Culver, Siegel, Stott, & Boas, 2003). Accurate results from both approaches depend on the use of realistic head models (Brigadoi, Aljabar, Kuklisova-Murgasova, Arridge, & Cooper, 2014; Fukui, Ajichi, & Okada, 2003). There are considerable brain structural changes during infancy through childhood and adulthood (Richards & Xie, 2015). Accurate models of DOT sensitivity must account for age-related changes in the head. The present study examined age-related changes in 1) scalp-to-brain distance, 2) the correspondence between scalp locations and anatomical regions, and 3) DOT sensitivity profiles. We used age-appropriate, realistic head models with extensive coverage of the infancy period (2 weeks through 2 years), two child ages (4, 12 years), and young adults (20 to 24 years).

Scalp-to-Cortex Distances Measured by Scalp Projection Methods

The initial step to understanding the underlying cortical structures being measured with NIRS is to measure the distance from the NIRS recording locations to the cortical surface. The 10-20, 10-10, and 10-5 systems provide a standardized and reproducible method for placing electrodes based on cranial landmarks and are often used to identify NIRS optode recording positions (Jurcak, Tsuzuki, & Dan, 2007). The electrode/optode locations are co-registered with structural MRIs to establish the recording sites on the scalp. Spatial scalp projection offers a method to link scalp locations to the underlying cortical structures (Tsuzuki & Dan, 2014). Spatial projections use an algorithm to project an electrode location on the scalp down to a location on the cortical surface (Okamoto & Dan, 2005). Adult studies projected 10-20 (Okamoto et al., 2004) and 10-10 electrodes (Koessler et al., 2009) to standard brain templates. Okamoto et al. (2004) found that the scalp-to-cortex distance was shallower in the frontal, temporal and occipital regions, but deeper in the parietal and along the intra-hemispherical fissure. Spatial scalp projection facilitates the understanding of the sampling depth required to measure the cortical activities using NIRS recording or DOT.

It is important to examine age-related changes in scalp-to-cortex distance. There is extensive brain morphological development from infancy to adolescence (Gilmore et al., 2011; Makropoulos et al., 2016; Richards & Conte, 2020; Richards & Xie, 2015). One change is the distance from the scalp to cortical landmarks (Heschl's gyrus, inferior frontal gyrus, frontal pole, occipital pole, parieto-occipital sulcus, and vertex). There are significant increases from newborn to age 12 (Beauchamp et al., 2011). Kabdebon et al. (2014) virtually placed 10-20 electrodes on individual MRIs from 3- to 17-week-old infants. The distance between the scalp electrode positions and the cortical surface decreased from the frontal to occipital locations. The pattern

was not observed in adult head models (Okamoto et al., 2004). Studies adopting the scalp projection method indicate that the scalp-to-cortex distance is smaller in infants (Emberson, Crosswhite, Richards, & Aslin, 2017; Kabdebon et al., 2014) and children (Whiteman, Santosa, Chen, Perlman, & Huppert, 2017) than in adults (Okamoto et al., 2004). Existing infant studies sampled a single age, or a narrow age range. Hence, there is insufficient information about the differences across age on overall scalp-to-cortex distance or scalp-to-cortex distance by electrode positions.

Scalp-location-to ROI Mapping Using Scalp Projection Methods

The spatial scalp projection method can also be used to identify the correspondence between scalp electrode locations and the underlying anatomical regions of interest (ROIs). The electrode-location-to-ROI mapping can be established first by transforming the individual's own MRI and electrode locations to a canonical average MRI template which has an anatomical stereotaxic atlas. Scalp electrode locations can then be projected to the cortical surface to identify to the corresponding ROI(s). Adult studies have demonstrated that there was a relatively consistent correspondence between the 10-20 (Okamoto et al., 2004) and 10-10 (Koessler et al., 2009) electrode positions and the underlying macro-anatomical ROIs. Greater inter-subject variations have been observed in O1 and O2 electrodes in the 10-20 system (Okamoto et al., 2004) and posterior central electrodes in the 10-10 system (Koessler et al., 2009). A methodological challenge in the ROI mapping is the limited availability of subjects' own MRIs. Co-registration methods for standalone DOT data have been developed so that electrode positions on the subject's scalp can be transformed to the space of reference MRIs in a database (Fekete, Rubin, Carlson, & Mujica-Parodi, 2011; Tsuzuki et al., 2012). The co-registration

methods result in similar results as using subjects' own MRIs (Tsuzuki et al., 2012; Tsuzuki & Dan, 2014).

Co-registering scalp electrode locations with reference MRIs is an effective method for identifying electrode-location-to-ROI correspondence in infants. One method is to project individuals' electrode locations to a template brain with ROI parcellations constructed from a representative infant or an average template based on infant MRIs. Kabdebon et al. (2014) transformed infants' (3 to 17 weeks) individual head models to a 7-week-old infant template and found stable correspondence between 10-20 electrode locations and underlying microanatomical ROIs. Electrodes O1, O2, T5 and T6 were projected to more inferior cortical regions than the cortical locations reported in Okamoto et al. (Okamoto et al., 2004). This study showed that age-related changes in the head and brain structures may lead to age-related variations in the correspondence between electrode positions and brain structures. Tsuzuki et al. (2017) transformed macroanatomical landmarks identified in 14 3- to 22-month-olds' MRIs to a 12-month-old template (Matsui et al., 2014) in reference to virtual 10-10 electrode locations (Jurcak et al., 2007). They found inter-subject variations in the relative positions among the microanatomical landmarks. However, the differences were smaller than the region defined by the 10-10 electrodes. Hence, there may be relatively stable electrode-location-to-ROI correspondence across ages. One important limitation of these studies is the use of a single individual or single-age template as a reference for age ranges across which significant brain development occurs (e.g. 3 to 17 weeks; or 3 to 22 months).

The use of individual MRIs or age-appropriate MRI templates and stereotaxic atlases for standalone DOT data can reduce errors in co-registration and provide more accurate representations of electrode-location-to-ROI correspondence. Lloyd-Fox et al. (2014) co-

registered channel locations (midway of between adjacent optode/electrode locations) on both the infants' (4.5- and 6-month-olds) own MRIs and the age-appropriate average templates from the Neurodevelopmental MRI Database (Richards, in prep; Richards, Sanchez, Phillips-Meek, & Xie, 2015; Sanchez, Richards, & Almli, 2012a, 2012b). Anatomical stereotaxic atlases were constructed for individuals' own MRIs and age-appropriate average templates (Fillmore, Richards, Phillips-Meek, Cryer, & Stevens, 2015). The correspondence between channel locations and ROIs in individual MRIs were highly comparable with the correspondence identified in the age-appropriate average MRI templates. An alternative to co-registering with the subjects' own MRIs or average templates is to use an MRI from another infant with similar head size and age. A series of functional near-infrared spectroscopy (fNIRS) studies adopted Lloyd-Fox et al. (2014)'s co-registration method and positioned optode locations on close-head-size individual MRIs (Lloyd-Fox, Wu, Richards, Elwell, & Johnson, 2013) or both close MRIs and age-appropriate average templates (Emberson, Cannon, Palmeri, Richards, & Aslin, 2016; Emberson et al., 2017; Emberson, Richards, & Aslin, 2015). Spatial scalp projection was used to establish probabilistic mappings between channel locations and atlas ROIs. The channels with a large probability of localizing to a target ROI were used for group-level analyses.

The Use of DOT Sensitivity to Describe Scalp-Cortex Correspondence

The use of spatial scalp projection for determining electrode-location-to-ROI correspondence is limited. It does not consider the interaction between near-infrared light and the optical properties of the biological tissues. Therefore, the approach is limited to spatially contiguous anatomical areas and cannot model directly the extent of the cortical regions being measured by NIRS recording nor the intensity of the signal generated by blood flow. An

alternative to the spatial scalp projection is to use DOT sensitivity patterns to determine the correspondence between scalp recording locations and underlying cortical anatomy.

The pattern of DOT distribution inside the head is often measured with Monte Carlo simulation methods that model the propagation of photons through heterogeneous tissue structures such as the human brain (Jacques & Wang, 1995). The inputs to Monte Carlo simulation are a segmented MRI that define tissue types, optical properties of the tissue types, simulated injection of light photons into the head, and an algorithm describing the path of the photon through the tissues. A computer program is used that takes this information and simulates the path of injected photons through the head media (e.g., (tMCimg; Boas et al., 2002); (MCX; Fang & Boas, 2009a); (MMC; Fang, 2010); (MCML; Jacques & Wang, 1995; Wang, Jacques, & Zheng, 1995) ; (TOAST++; Schweiger & Arridge, 2014)).

The output from the Monte Carlo simulation program is a distribution of photon travel across the head, and DOT sensitivity can be quantified from Monte Carlo simulation outputs. The DOT sensitivity is conceptualized as the extent to which the detected signal is influenced by changes in optical properties in the given region of tissue (Mansouri, L'Huillier, Kashou, & Humeau, 2010). One representation of DOT sensitivity is the spatial sensitivity profile. The profiles depict the fluence distribution of detected photons (Boas et al., 2002). We will call the fluence distribution for source-electrode location “Direct DOT” ("2-point Green's function"; Strangman, Li, & Zhang, 2013). A second approach to quantify DOT sensitivity is to use the photon measurement density function (PMDF). The PMDF quantifies optical sensitivity in NIRS source-detector recording by calculating the product of the fluence distribution at the source location and the detector location (PMDF; Brigadoi et al., 2014; Brigadoi & Cooper, 2015; or "3-point Green's function"; Strangman et al., 2013). We will call this the “Source-Detector Channel

DOT" (S-D Channel DOT). S-D Channel DOT represents the probability that a photon injected from the source and measured at the detector location has propagated through a given tissue. DOT sensitivity is quantified as each location at which a photon traverses through a given tissue region, or "partial path length" (PPL; Mansouri et al., 2010; Strangman, Zhang, & Li, 2014; Wang, Ayaz, & Izzetoglu, 2019). PPL represent the penetration depths of the photon measured in the medium (Mansouri et al., 2010).

The DOT sensitivity profile provides a measure of the scalp-location-to-ROI correspondence. The sensitivity distribution can be used to estimate the distance from scalp locations to the surface of cortical regions that are *measurable* with DOT and localize the ROIs that would be sampled with NIRS. For example, Haeussinger et al. (2011) showed that the average distance from scalp channel locations to the cortical surface that could be sampled by the channel sensitivity distribution was 14.5±1.4 mm in adults. Studies have estimated DOT sensitivity in head models with atlas parcellations in infants (Bulgarelli et al., 2019; Bulgarelli et al., 2020; Perdue et al., 2019), children (Whiteman et al., 2017) and adults (Zimeo Morais, Balardin, & Sato, 2018). These studies computed the channel-ROI correspondence and generated look-up tables to show channel-ROI probabilities. Zimeo Morais et al. (2018) constructed 130 source-detector channels from 10-10 electrode pairings and computed the specificity of each channel to the corresponding ROIs using the S-D Channel DOT measure. Such look-up tables facilitate the optimization of channel array design to maximize DOT sensitivity to user-specified ROIs (Brigadoi, Salvagnin, Fischetti, & Cooper, 2018; Zimeo Morais et al., 2018) and help to localize the possible ROIs that generated the fNIRS signals (Bulgarelli et al., 2019; Bulgarelli et al., 2020; Perdue et al., 2019).

DOT Sensitivity Profile by Source-Detector Separation Distances

The DOT sensitivity changes as a function of source-detector separation distances (Mansouri et al., 2010; Strangman et al., 2013; Strangman et al., 2014; Wang et al., 2019). As the source-detector distance increases, the fluence distribution covers wider tissue regions, extends deeper into the brain, and decreases in DOT sensitivity. For example, it has been found that for 20 mm source-detector separation the fluence distribution was largely confined to shallow layers of the head model and about 6% of the total sensitivity was attributed to the brain (gray and white matters) (Strangman et al., 2013; Strangman et al., 2014). Sensitivity to the brain increased linearly from 20 mm up to 45 mm separation (Mansouri et al., 2010; Strangman et al., 2013; Strangman et al., 2014; Wang et al., 2019). The increase in sensitivity to the brain was less steep at larger distances (Strangman et al., 2013; Strangman et al., 2014). There was a trade-off between penetration depth and signal intensity. Signal intensity decreased monotonically and exponentially with increased depth at all separation distances (Strangman et al., 2013). Wang et al. (2019) showed that the signal strength was reduced as source-detector separation increased. Hence, the optimal separation distances for measuring brain activity need to be determined based on the consideration of depth sensitivity, the desired spatial resolution of the measurement regions, and the achievable signal strength for the measurement device.

There are developmental effects in DOT sensitivity. Age was positively associated with the depth sensitivity in the frontal and occipital regions in head models of children between 5 to 11 years old (Whiteman et al., 2017). Fukui et al. (2003) compared DOT sensitivity by separation distances in neonates (20-24 weeks) and adults. They found that the sensitivity to brain tissues was greater in neonates than adults across all separation distances (10 mm to 60 mm). Additionally, there was an age-by-separation effect. Larger source-detector separations

(from 40 mm to 50 mm) extended the penetration of the fluence distribution to the grey matter in neonates but did not increase the penetration depth in the adult head model. Age differences in DOT sensitivity may be attributed to anatomical variations across ages. Increased scalp-to-brain distance was related to reduced path length through the brain regions in children (Whiteman et al., 2017). Moreover, greater scalp and skull thickness was associated with reduced sensitivity to the gray matter across source-detector separations from 20 mm to 50 mm in adults (Strangman et al., 2014). These studies conclude that age-related changes head/brain anatomy and composition affect the DOT sensitivity function. However, these studies are based on a limited range of ages (e.g., neonate; 5 to 11 years) and do not cover the age span across infancy when dramatic development of the head and brain occur.

The Present Study

The current study examined age-related variations in the scalp-cortex correspondence and DOT sensitivity profiles. Our primary contribution was to use existing methods for DOT sensitivity across the period of infancy (2 weeks through 24 months) with narrow age bands, and compare these to older children (4, 12 years) and adults (20-24 years). Spatial scalp projection was used to estimate the distances between scalp electrode and channel locations and the cortical surface. We projected the electrode location to atlas locations delineated on individual MRIs to identify the anatomical mapping between scalp and ROI locations. We used the MCX photon migration simulation program to model photon propagation through the segmented tissues in the individual head MRIs (Fang & Boas, 2009a; see Supplemental Information for further information). We estimated fluence distributions from the simulations. We computed the distance between scalp locations and the cortical locations with maximum fluence. We provided a look-up table to present the probabilistic mapping between scalp channel locations and the

underlying anatomical ROIs. Lastly, we depicted changes in DOT sensitivity profiles as a function of source-detector separation distances. The present study has important implications in the design of developmentally-sensitive channel placements for NIRS recordings.

Method

Participants

The participants were 1058 typically developing participants ranging from 2 weeks to 24 years of age. The MRIs were obtained from open-access databases and a local scanning facility. The sample consisted of 9 participants (4 females) from the Autism Brain Imaging Data Exchange (ABIDE; Di Martino et al., 2014), 280 (143 females) from the Baby Connectome Project (BCP; Howell et al., 2019), 177 (93 females) from the Early Brain Development Study (EBDS; Gilmore et al., 2010), 282 (106 females) from the Infant Brain Imaging Study (IBIS; e.g. Hazlett et al., 2017), 14 (5 females) from the Pediatric Imaging, Neurocognition, and Genetics Data Repository (PING; Jernigan et al., 2016), and 296 scans (141 females) from data collected at the McCausland Center of Brain Imaging (MCBI) or drawn from collaborative studies at other sites. Table 1 presents the number of MRIs for the open access databases, separately for age and gender. The sample ages were narrowest in the infancy period (2 weeks, 1-, 1.5-, 3-, or 6-month intervals from 2 weeks through 2 years), and included exemplar ages in children and adolescent ages (4, 12 years) and adult (20-24 years). All studies had institutional review board approval and informed consent for participants.

MRI Sequences

The present study utilized T1-weighted (T1W) and T2-weighted (T2W) scans from each collection site. Details of the MRI acquisition protocols have been described in literatures on the Neurodevelopmental MRI Database (Fillmore, Phillips-Meek, & Richards, 2015; Fillmore,

Table 1. Demographical information of study participants by age group, sex, and data source.
Note. ABIDE=Autism Brain Imaging Data Exchange; BCP=Baby Connectome Project; EBDS=Early Brain Development Study; IBIS=Infant Brain Imaging Study; MCBI=McCausland Center for Brain Imaging; PING=Pediatric Imaging, Neurocognition, and Genetics Data Repository

Participant Information			**Data Source**					
Age Group	**Total *N***	**Female *N***	**ABIDE *N***	**BCP *N***	**EBDS *N***	**IBIS *N***	**MCBI and Collaboration Sites *N***	**PING *N***
2 Weeks	41	24	0	3	38	0	0	0
1 Month	96	40	0	17	79	0	0	0
2 Months	68	40	0	8	60	0	0	0
3 Months	38	21	0	24	0	0	14	0
4.5 Months	54	29	0	41	0	0	13	0
6 Months	74	35	0	0	0	60	14	0
7.5 Months	61	17	0	0	0	49	12	0
9 Months	60	35	0	48	0	3	9	0
10.5 Months	42	21	0	40	0	0	2	0
12 Months	109	36	0	0	0	89	20	0
15 Months	78	41	0	63	0	8	7	0
18 Months	76	31	0	36	0	8	32	0
2 Years	74	22	0	0	0	65	1	0
4 Years	24	9	0	0	0	0	10	14
12 Years	37	14	9	0	0	0	28	0
20-24 Years	134	77	0	0	0	0	134	0

Richards, et al., 2015; Richards, in prep; Richards, Sanchez, et al., 2015; Sanchez et al., 2012a, 2012b). All MRIs were converted to NIFTI compressed format with 32-bit floating point resolution. Bias-field inhomogeneity correction (N4 algorithm) was performed on the extracted T1-weighted images (Avants et al., 2011; Tustison et al., 2010).

MRI Preprocessing and Segmentation

First, the brains were extracted from the whole-head MRI volume in a procedure adapted from the FSL VBM pipeline (Douaud et al., 2007). The T1W volume for each participant was registered to an age-appropriate average MRI template. The MRI templates came from the Neurodevelopmental MRI database (Richards, Sanchez, et al., 2015; Sanchez et al., 2012a, 2012b). The brain from the average template was transformed into the participant MRI space and used a mask on the head volume. The extracted masked data was then used with the FSL brain extraction tool program (Jenkinson, Pechaud, & Smith, 2005; Smith et al., 2004). Each brain was visually inspected and manually modified if necessary.

Second, each head MRI volume was segmented into 9 or 10 media types: gray matter (GM), white matter (WM), cerebrospinal fluid (CSF), non-myelinated axons (NMA), other brain matter, skin, skull, air, eyes, and other inside skull material. The FSL FAST procedure (Zhang, Brady, & Smith, 2001) was used to segment the T1-weighted images into GM, WM, or other matter (OM). The GM regions was further separated into gray matter and non-myelinated axons for infants 12 months of age or younger by using the pattern of GM/WM in the average MRI template from two-year-olds as a probability map and identifying participant GM as probable GM or NMA. The CSF was identified in the T2W images using a threshold procedure. The CSF was removed from the materials from the FAST procedure, with the remainder defined as GM, WM, NMA or other inside skull material. The BETSURF procedure (Jenkinson et al., 2005;

Smith et al., 2004) was used with the extracted brain, T1W and T2W volumes, to identify skull and scalp regions. The nasal cavity and eyes were identified manually using MRIcron (Rorden, 2012; Rorden & Brett, 2000). Finally, any other matter inside the head volume not defined as above was defined as “other inside skull material”. This generally was in the region of the neck and consisted primarily of muscle and secondarily of spinal bone. These segmented regions were assembled into a single MRI volume we will refer to as the “segmented head MRI volume”. Figure 1A shows a 3D rending of the T1W volume from a 3-month-old infant with a cutout revealing the segmented MRI volume. The realistic head model represents the geometry of the head and allow us to differentiate optical properties of different tissue types.

Mesh Generation

A “finite element method” (FEM) tetrahedral mesh was constructed from the segmented head MRI volume. Figure 1B and 1C displayed meshes that were produced using the iso2mesh toolbox with CGAL 3.6 mesh program ("v2m" function, Fang & Boas, 2009b). Tetrahedral meshes accurately represent boundaries of complex three-dimensional volumetric tissues and increase the accuracy in modeling photon propagation in the complex mediums such as the head and brain (Yan, Tran, & Fang, 2019). The FEM volumetric meshes have nodes that represent the voxel locations for the tetrahedra, a 4-element matrix representing the corners of each tetrahedron, and a vector representing the media type from the segmented head MRI volume. A mesh was generated for each segmented head MRI volume. Figure 1B depicts an example of the dense meshes. The number of nodes, elements, and tetra volume were calculated for the infants (2 weeks through 2 years), children (4 and 12 years), and adults (Supplemental Figure 1). The average number of nodes was 301263, 417523, 440384, for the infants, children, and adults, respectively; average number of elements was 1,752,221, 2,449,375, and 2,582,646; and average

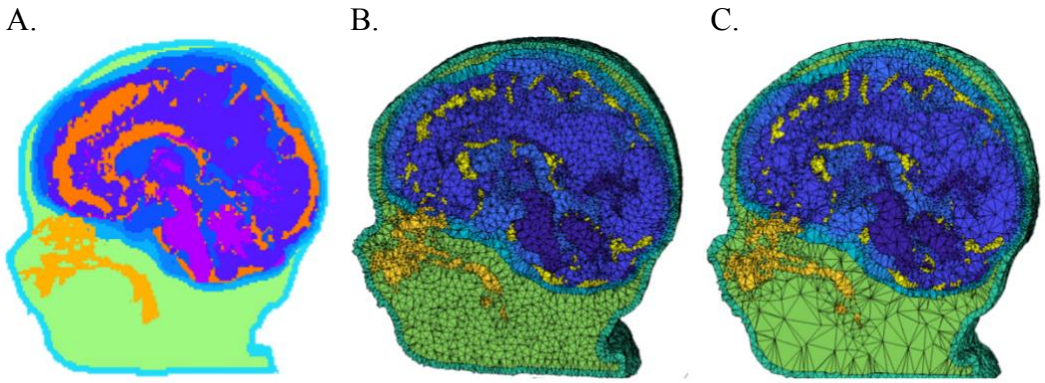

Fig 1. Segmented head MRI volumes. The examples were taken from the same 3-month-old infant MRI. A. The segmented head model. Aqua is the skull, purple is the gray matter, magenta is the white matter, dark orange is the cerebrospinal fluid, light blue is the dura, light orange is the nasal and mouth air cavities, and green is the non-bone structure (muscle, sinew, fat). B. The segmented head model with dense finite element model (FEM) mesh. C. The segmented head model with sparse FEM mesh.

tetra volumes were 21, 22, and 27 cubic mm. The change in node and element size reflect increases in head size over these ages. We will refer to this as the "segmented FEM mesh". We used the mesh to locate points on the scalp that were closest to the electrode positions, and for the segmented FEM mesh for the MMC computer program.

Scalp Locations

Virtual Electrodes Placement

The locations for the 10-10 and 10-5 electrode systems were constructed on each head MRI volume. First, we manually marked cranial fiducial points using MRIcron (Rorden, 2012; Rorden & Brett, 2000): nasion (Nz), vertex (Vz), inion (Iz), left preauricular point (LPA), right preauricular point (RPA), left mastoid (LMa), and right mastoid (RMa) (Richards, Boswell, Stevens, & Vendemia, 2015). The coordinates of the fiducials were transferred on to the scalp mesh. Next, we calculated 81 virtual electrode positions based on the "unambiguously illustrated 10-10 system (Jurcak et al., 2007). Details for constructing the 10-10 locations are described in Richards, Boswell, et al. (2015) and the Supplemental Information. We simulated a total of 358 electrodes on 10-5 locations by calculating center points between 10-10 positions. The electrode positions also were computed for the average MRI templates. Figure 2 illustrates the placements of 10-10 and 10-5 electrodes positions.

Source-Detector Channels, All Electrode Pairs

Source-detector channels were defined in three ways for the analyses. *Source-Detector Channels*: Source-detector channel locations were defined for some analyses using electrode combinations centered on each 10-10 electrode. The 10-10 electrode locations were centered between surrounding adjacent pairs of 10-10 or 10-5 electrode locations. There were 251 source-detector pairs formed with adjacent 10-10 electrodes, $Mean_{\text{Separation}} = 57.95$ mm; $SD = 14.22$, and

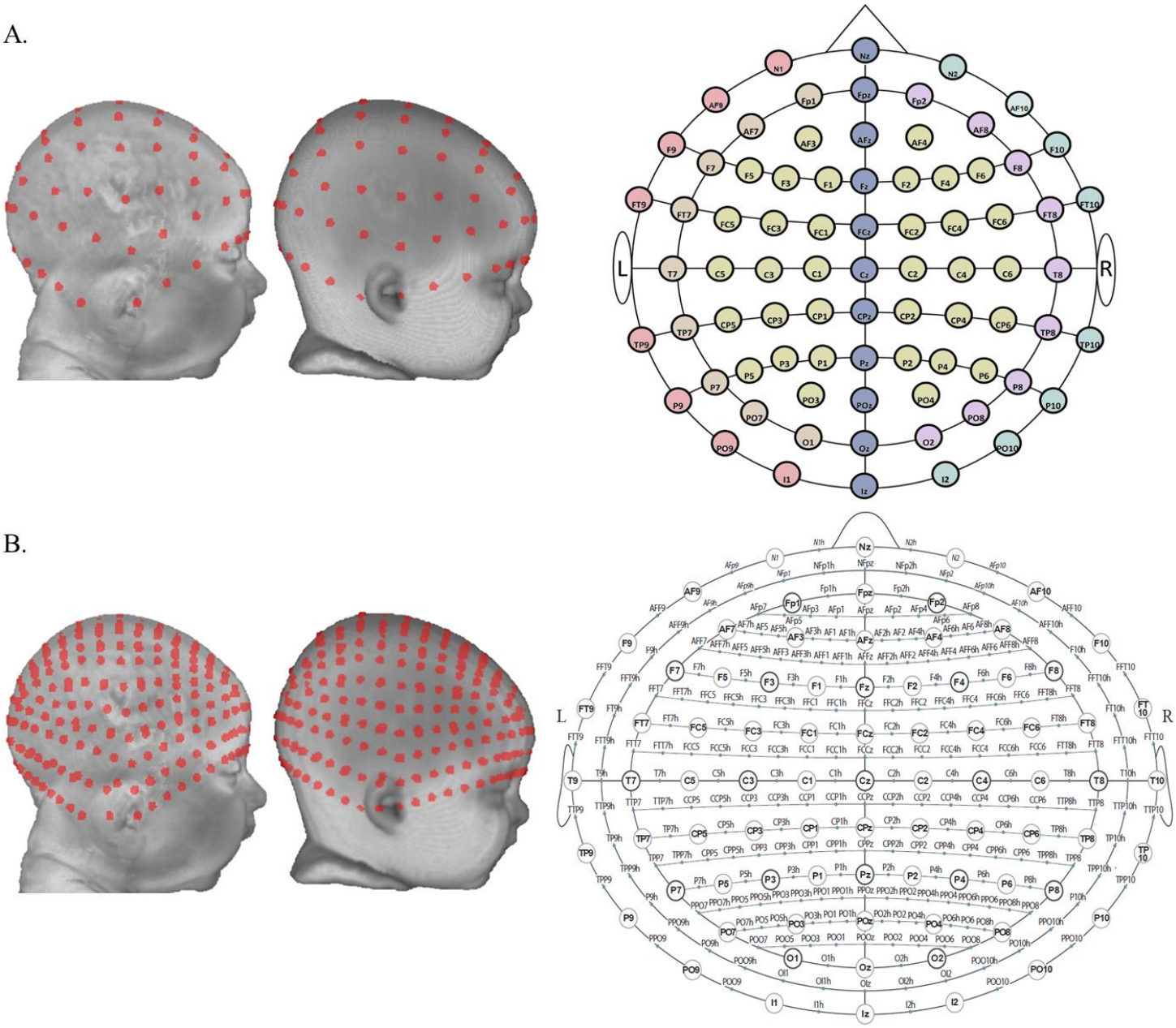

Fig 2. Virtual electrode placement. A. Ten-ten virtual electrode placement. From left to right: a three-month individual head model, an average template for three-month-olds, and a two-dimensional layout of the 10-10 system). Ten-ten electrodes were divided into six groups for visualization purposes. The six groups were color-coded on the two-dimensional schematic of the 10-10 system. Group 1: electrodes on the central curve (Nz-Cz-Iz). Group 2: electrodes on the left curve between Nz and Iz (N1-LPA/T9-I1). Group 3: electrodes on the right curve between Nz and Iz (N2-RPA/T10-I2). Group 4: electrodes on the left curve between Fpz and Oz (Fp1-T7-O1). Group 5: electrodes on the right curve between Fpz and Oz (Fp2-T8-O2). Group 6: the remaining electrodes enclosed by the central curve, the left and right curves between Fpz and Oz. B. Ten-five virtual electrode placement. From left to right: the same three-month individual head model, the three-month average template, and a two-dimensional layout of the 10-5 system (Jurcak et al., 2007).

251 pairs formed with adjacent 10-5 electrodes, $Mean_{Separation} = 28.92$ mm; $SD = 7.06$. *All Electrode Pairs*: Some channel locations were defined from the combination of all 10-5 electrode positions for the source-detector distance analyses. The path from each electrode to all other electrodes was traced on the scalp and the distance of the path recorded (63,903 paths). The channel location was defined at the half-way point in this path, and the electrode pairs, scalp path distance, and channel location were recorded.

Cortical Locations

Three stereotaxic atlases were constructed for each individual MRI. The atlases delineate cortical lobes or more specified locations within the lobes. We created a 1.5 cm spherical mask around each electrode or channel location to standardize the region to be identified in the atlases. The atlases and spherical masks were used with the spatial scalp projection method (described below) to describe the correspondence between scalp electrode positions and corresponding cortical structures in the individual's own brain space with various spatial resolution (Lloyd-Fox et al., 2014). They were also used with the "S-D Channel DOT" estimates (described below) to identify the anatomical structures being sampled by the fluence distribution.

Stereotaxic Atlases

Three atlases were constructed for each individual MRI to delineate anatomical regions that can be used to identify brain locations corresponding to scalp electrode positions or DOT sensitivity patterns. Details of the atlas constructions may be found elsewhere (Fillmore, Richards, et al., 2015; Lloyd-Fox et al., 2014; Richards, 2013). The first atlas was the LONI Probabilistic Brain Atlas (LPBA40; Shattuck et al., 2008), which contains 56 areas from the cortical and subcortical regions, brainstem and cerebellum. The second was the Hammers atlas, based on MRIs from the IXI MRI database (Heckemann, Hajnal, Aljabar, Rueckert, & Hammers,

2006), consists of 83 areas defined from the cortex, subcortical, brainstem and cerebellum (Gousias et al., 2008). We used a majority vote fusion procedure that combines labeled segments from manually segmented MRIs to produce atlases that identify an anatomical area for each brain voxel of the individual MRI. The third atlas was an automatically constructed lobar atlas that identifies the major cortical lobes (e.g. frontal), some sublobar cortical (e.g. fusiform gyrus), subcortical (e.g. striatum), cerebellum and brainstem. The atlas was constructed by extracting and combining common areas from the LPBA40 and Hammers atlases, and manually segmented average template atlases transformed from the template space to the individual MRI space.

Spherical Masks

We created a sphere with 1.5 cm radius around each 10-10 electrode and channel location. Figure 3 shows examples of the spherical volumes were used as masks for determining the correspondence between scalp and brain locations. We identified the atlas regions of interest (ROIs) that intersected with the masks and computed the voxel numbers in the sphere of these ROIs. Hence, there was a distribution of atlas ROIs with various voxel numbers that were mapped to each electrode and channel location.

Photon Migration Simulations

The DOT fluence values were estimated with photon migration simulations. We modeled photon migration through brain tissues using the Monte Carlo eXtreme package (MCX; Fang & Boas, 2009a; Fang & Yan, 2019). The package implements an GPU-accelerated, voxel-based Monte Carlo simulation algorithm. We launched 10^8 photons for the time window of 0 to 5 nanoseconds. The fluence resolution was 50 time-gates (Zimeo Morais et al., 2018). The wavelength was set at 690 nanometers. Photons were sent from the 358 10-5 electrode positions. The optical properties of the 10 tissue types were set in accordance with previous studies by

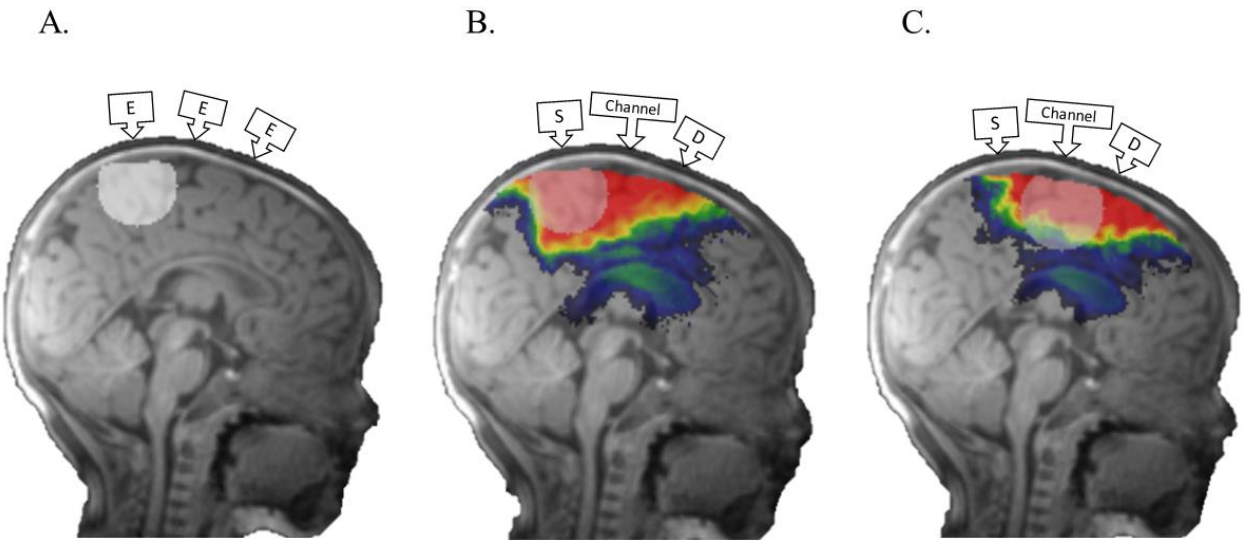

Fig 3. Methods for determining scalp-location-to-ROI mapping. The MRI was taken from a 3-month infant. A. An example of a 1.5cm-radius spherical mask created around an electrode location for the spatial scalp projection procedure. B. An illustration of a spherical mask created around a source location for the Direct DOT procedure. C. An illustration of a spherical mask created around a channel location for the Source-Detector (S-D) Channel DOT procedure. Monte Carlo photon migration simulations were used to estimate fluence distributions for individual 10-5 electrode locations (Direct DOT) and 10-10 channel locations (S-D Channel DOT). The red area represents greater fluence.

Perdue et al. (2019) and Fang (2010) which came primarily from Strangman, Franceschini, and Boas (2003) and Yaroslavsky et al. (2002). Table 2 contains the values that were used. It should be noted that there has been no consensus on the optical properties in the literature (Zimeo Morais et al., 2018). The values differ considerably across studies (Boas et al., 2002; Brigadoi & Cooper, 2015; Custo et al., 2010; Strangman et al., 2003; Strangman et al., 2013; Whiteman et al., 2017; Zimeo Morais et al., 2018). It is likely that different values are needed for adults versus developmental samples (Fukui et al., 2003). We have compiled optical properties used in published studies in Supplemental Information table 2.

The Monte Carlo simulations estimate fluence distribution (Boas et al., 2002; Strangman et al., 2013). The photons were injected at the electrode position. The "flux" strength of the photons, or "fluence" of the sum photon flux, decreased monotonically due to absorption and scattering as photons traveled through brain tissues. The simulations accounted for absorption, scattering and reflection based on the specified optical properties (Boas et al., 2002; Fang & Boas, 2009a). Each simulation continued until the photon exited the media, was absorbed by the media, or after 5 nanoseconds. The output of the simulations included the photon fluence at each nanosecond for each voxel from the injected photons. The number ranged from zero to the total number of injected photons. We summed this value across the 5 nanoseconds of the simulation. This value represents the fluence of the simulation. We took the log (fluence) as our number representing the DOT sensitivity for each voxel. Figure 3B shows the DOT fluence plotted on an individual subject MRI for a single electrode location. The gradual monotonic decrease in fluence as a function of partial path length may be seen in this figure.

Table 2. Optical properties used in Monte Carlo photon migration simulations. μ_a is the optical absorption coefficient; μ_s is the scattering coefficient, g is the anisotropy coefficient, and N is the index of refraction.

Tissue Type	μ_a **(mm^{-1})**	μ_s **(mm^{-1})**	g	N
White matter	0.07	40.1	0.85	1.37
Gray matter	0.02	8.4	0.90	1.37
CSF	0.0004	1	0.99	1.37
Dura	0.0101	80	0.99	1.37
Skull	0.0101	100	0.99	1.37
Skin	0.0101	80	0.99	1.37
Muscle	0.0101	80	0.99	1.37
Eyes	0.0004	1	0.99	1.37
Nasal Cavity	0.0101	80	0.99	1.37
Non-myelinated Axons	0.07	40.1	0.85	1.37

DOT Sensitivity Analyses

The output from the Monte Carlo simulation contained the fluence across the entire MRI volume separately for each electrode. We simulated the path for several analyses from a source-electrode (optode) to a detector-electrode (optode). This was done by multiplying the source-electrode (optode) fluence distribution by the detector-electrode (optode) fluence distribution. We will refer to this as “S-D Channel DOT fluence”. This represents the DOT fluence sensitivity for a photon channel from the source to the detector ("PMDF" in Brigadoi & Cooper, 2015). An ad-hoc method has been used in some studies to divide the product by the estimated value of the photons from the source in the vicinity of the detector (Perdue, Fang, & Diamond, 2012). This step was not taken in the current study. Figure 3C shows the S-D Channel DOT fluence plotted on an MRI for a single source-detector pair. This figure shows a similar monotonic decrease in fluence strength as a function of partial path length.

Spatial Scalp Projection

We performed spatial projections from each 10-10 or 10-5 electrode position on the scalp to the brain surface. These projections were used to measure the distance between each scalp electrode and the brain surface and to examine electrode scalp location to anatomical ROI correlation (Emberson, Cannon, et al., 2016; Emberson et al., 2017; Emberson et al., 2015; Lloyd-Fox et al., 2014; Lloyd-Fox et al., 2013). The brain locations underlying each electrode was determined by an algorithm in which a spatial projection from the electrode scalp surface to the brain center was done. The point where the projection intersected the cortex was identified. These projections were done with the scalp and brain elements of the segmented FEM mesh and mesh manipulation tools from the iso2mesh toolbox (Fang & Boas, 2009b).

Scalp-to-cortex Distance

We compared the distance from scalp electrode or channel locations to cortical surface across age groups. The "Scalp Projection" was simply the closest intersection of the brain from the projection of the electrode position toward the brain. The "Direct DOT" distance was based on the single-electrode DOT fluence. A 1.5 cm radius spherical mask was created at the point where the spatial projection intersected the brain. The maximum DOT fluence in the brain masked by the sphere was used as the location to calculate the Direct DOT distance. The "S-D Channel DOT" distance was based on the source-detector S-D Channel DOT fluence. The same spatial projection from the electrode, and the 1.5 cm sphere, was applied to the S-D Channel DOT fluence and the location of the maximum S-D Channel DOT fluence was used to calculate the S-D Channel DOT distance.

Scalp-location-to-ROI Mapping

The Scalp Projection, Direct DOT and the S-D Channel DOT sensitivity were used to generate a look-up procedure that links the scalp electrode or channel locations to the lobar, Hammer, and LPBA40 atlas ROIs. A 1.5 cm mask was placed on the scalp projection to the brain intersection, maximum point of the DOT fluence, or maximum point of the S-D Channel DOT fluence. Figure 3A shows a sphere surrounding the scalp projection to the brain intersection; Figure 3B shows a sphere surrounding the electrode to the max DOT fluence location; Figure 3C shows a sphere surrounding the electrode to the S-D Channel DOT fluence. The anatomical ROI of each voxel in the respective spheres were recorded. The percentage of voxels in each ROI that intersected with the spherical masks was computed. We created tables for each age that listed the ROIs and the percentage of voxels in each ROI that intersected with the spherical masks created around the 10-10 electrode (Scalp Projection) and channel locations

(S-D Channel DOT). The Scalp Projection look-up table details the spatial correspondence between the scalp electrode location and anatomical brain regions. The S-D Channel DOT look-up table illustrates the channel DOT sensitivity to cortical regions.

Depth Sensitivity Profile by Source-Detector Separation Distances

We examined how the depth sensitivity of S-D Channel DOT changed as a function of source-detector separation distance. The target source-detector separation distances for testing were from 10 mm to 60 mm by 5 mm increments. The S-D DOT fluence sensitivity function was defined as the fluence value at the voxel as a function of the distance (depth) from the channel location to the voxel (PPL; Mansouri et al., 2010; Strangman et al., 2014; Wang et al., 2019). We additionally assessed the variance of the sensitivity profile by examining the standard error of the mean fluence value as a function of PPL. The shape of the S-D DOT fluence distribution was quantified by the half-width half-maximum (HWHM; Kumar Reddy & Sagar, 2015). The HWHM identified the PPL location at which the fluence first dropped below half of the maximum value. We referred to this as the HWHM location.

Additional Measures and Analyses

There were several methods and results that are presented in the Supplemental Information. These include tMCimg (Boas et al., 2002) simulations in all individual MRIs and age-appropriate average templates and MMC simulations (Fang & Yan, 2019; Tran, Yan, & Fang, 2020; Yan et al., 2019) in 3-month and 6-month old individual MRIs and average templates. We computed the Direct DOT and S-D Channel DOT distances using the photon fluence estimated from the simulations. We compared the scalp-to-cortex distance estimations obtained from the MCX, tMCimg, and MMC simulation packages. *fOLD Channels*: We used a set of electrode pairs to define source-detector channels from the 130 channel locations specified

in the fNIRS Optodes' Location Decider (fOLD) (Zimeo Morais et al., 2018). The actual computation of the DOT fluence channels came from the "All Electrode Pairs" combinations specific to the fOLD channel. We computed S-D Channel DOT fluence in selected age groups (3 month, 6 month, and 20-24 years) for the 130 channel locations specified in the fOLD toolbox (Zimeo Morais et al., 2018) using fluence estimated from MCX simulations. We provided a look-up table that presented the specificity of each fOLD channel to the underlying ROI(s). We also compared scalp-to-cortex distances among simulation methods and brain model types.

Results

Scalp-to-Cortex Distance

We examined age-related changes in scalp-to-cortex distance. Figure 4 shows 2-D scalp topographical maps plotted with the Scalp Projection distance represented by the color map separately by age, and 3-D renderings of the distance on the head for three selected ages. There was an increase in the distance across electrode positions from the infants to the children to the adults. The frontal and central electrodes on the bottom row (N1, AF9, F9, FT9, T9/LPA, TP9, N2, AF10, F10, FT10, T10/RPA, and TP10) showed the largest scalp-to-cortex distance, followed by the frontal and midline electrode positions, then followed by electrodes over the temporal, parietal and occipital positions. The shift from the frontal-midline electrodes to the other scalp positions was most evident in the 3- to 10.5-month-old groups. Figure 5 shows 2-D maps and 3-D renderings for the S-D Channel DOT scalp-to-cortex distance. The distance of the maximum S-D Channel DOT fluence was larger than the Scalp Projections distance at all ages (cf. Figure 4, 5). A similar pattern of distances across the scalp was found with the S-D Channel DOT and the Scalp Projection distance. These included the change in distance over age and the bottom row to frontal-midline-temporal/parietal/occipital distance for the youngest ages. The

A.

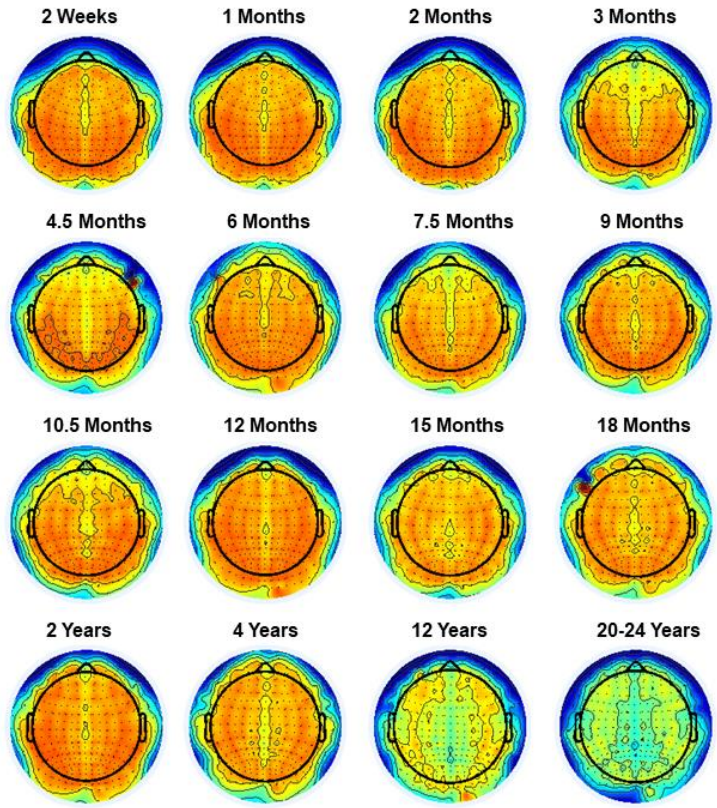

B.

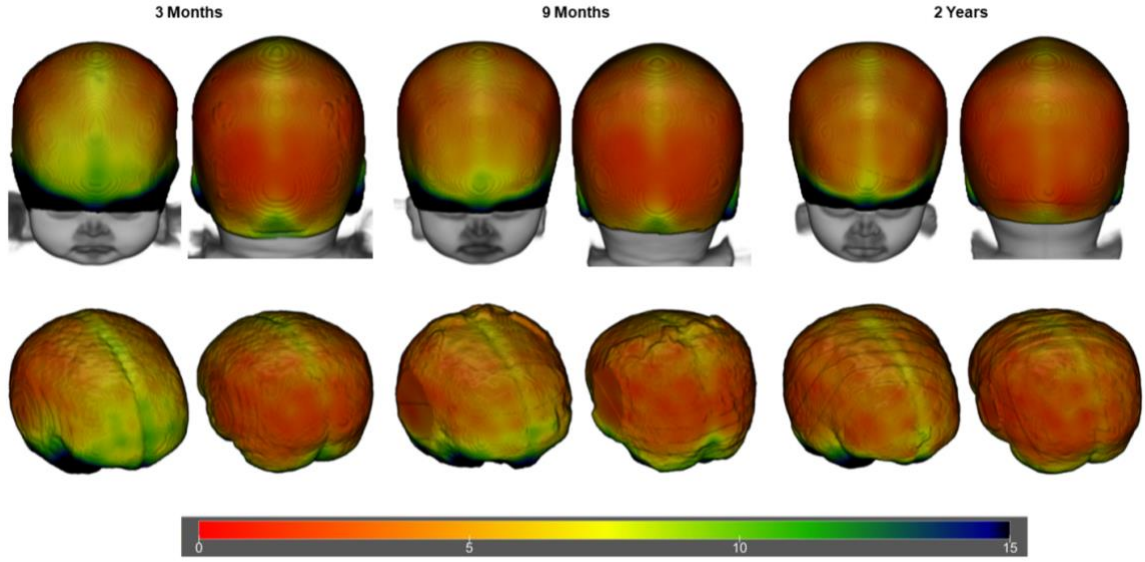

Fig 4. Mean distance from the scalp to cortical surface by electrode locations estimated using scalp projection. For the visualization purpose, estimations for the 10-5 electrode locations were displayed. A. Scalp topographical maps for all age groups. Darker red represents closer scalp-to-cortex distances, and darker blue indicates greater distances. B. Three-dimensional rendering of mean distances on the heads (top row) and on the brains (bottom row) at 3-month, 9-months, and 2-years, selected as examples. Head and brain models were generated using age-matched average templates.

A.

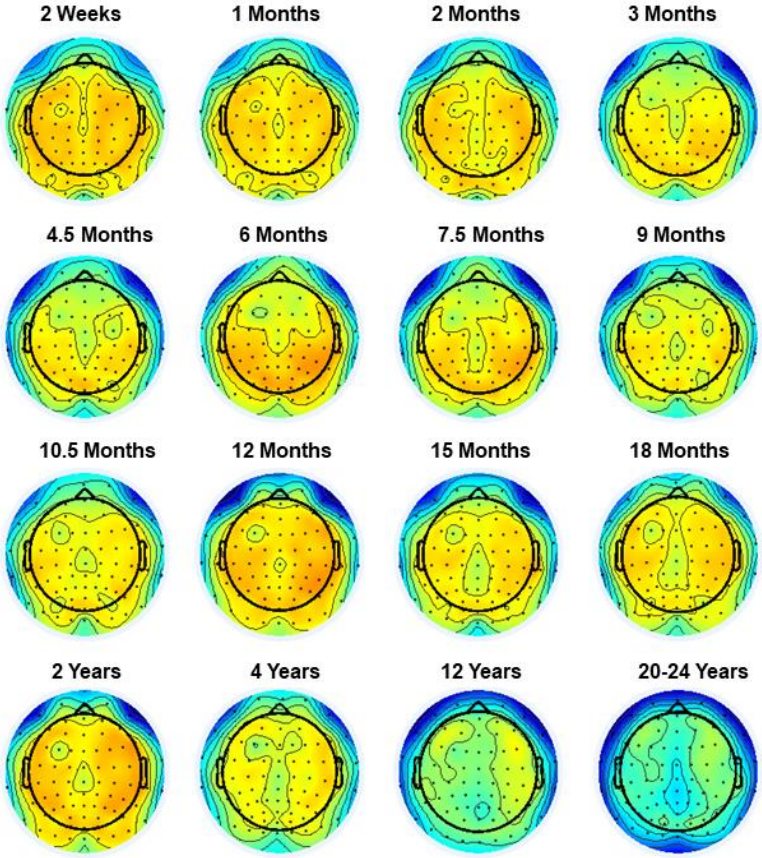

B.

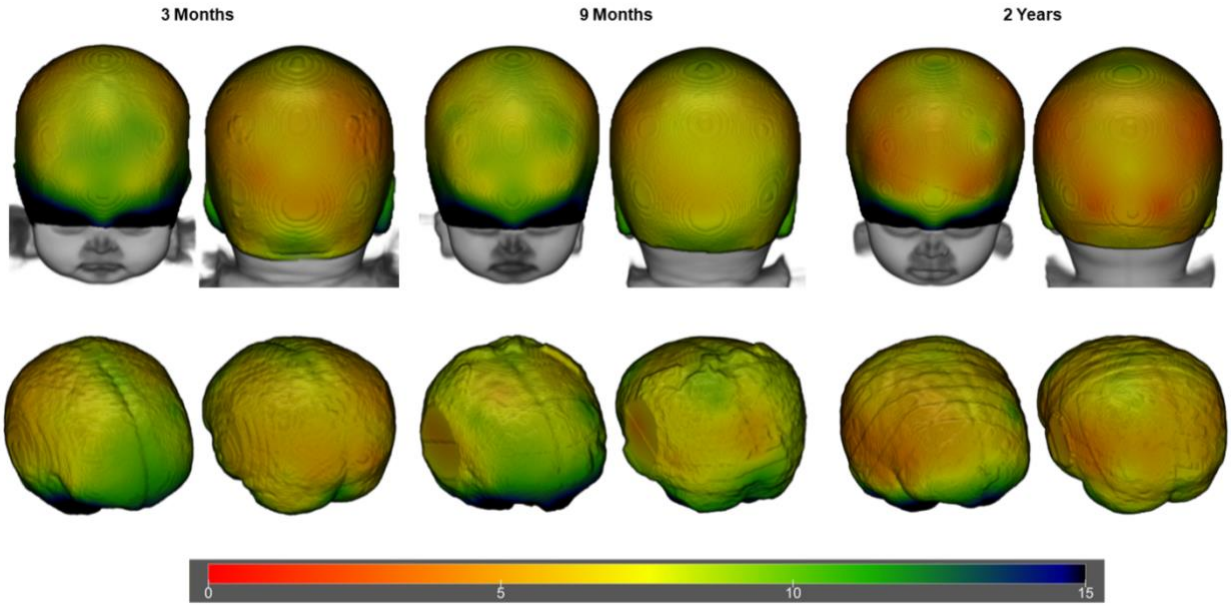

Fig 5. Mean S-D Channel DOT distances at 10-10 channel positions. A. Scalp topographical maps for all age groups. Darker red represents closer scalp-to-cortex distances, and darker blue indicates greater distances. B. Three-dimensional rendering of mean distance on the heads (top row) and on the brains (bottom row) at 3-month, 9-months, and 12-years, selected as examples. Head and brain models were generated using age-matched average templates.

anterior-to-posterior decreases in scalp-to-cortex distance were visible in most of the age groups (2 weeks to 10.5 months, 15 months, and 18 months).

We inspected changes in the scalp-to-brain distances across the individual 10-10 electrode positions. The distance measures were averaged across three age groups (infants and toddlers: 2 weeks to 2 years; children: 4 years and 12 years; and adults: 20-24 years), electrode position, and estimation methods (Scalp Projection, Direct DOT, and S-D Channel DOT). Figure 6A shows the scalp-to-cortex distances for the 10-10 positions separately for the three age groups and the three estimation methods. The larger distance of the bottom row was most obvious in these figures for all age groups. This was followed by the midline electrodes and then by the electrodes in the other positions. The distances in Figure 6A were based on averaging the distances from the MRIs of all participants in the age group. Figure 6B displays the mean S-D Channel DOT distances for the infant and toddler, child, and adult group averaged across the 81 channel positions and individual age groups. We also found that the distances for the S-D Channel DOT fluence for the participant-based averages (e.g., Figure 6A) were similar to the distances calculated from the average MRI template for the same age (Supplemental Information Figure 4A).

The scalp-to-cortex distances were analyzed as a function of age for the Scalp Projection and S-D Channel DOT estimation methods. A one-way ANOVA for the infant ages (13: 2 weeks through 2 years) was computed separately for the distances from the three estimation methods. The data for the frontal-central positions on the bottom row were excluded from this analysis. There were significant main effects of age on the Scalp Projection, F (12, 856) = 19.11, $p < .001$, Direct DOT, F (12, 849) = 26.93, $p < .001$, and S-D Channel DOT distance measures, F (2, 849) = 26.71, $p < .001$. Figure 7 shows the average scalp-to-cortex distances for the age groups for the

A.

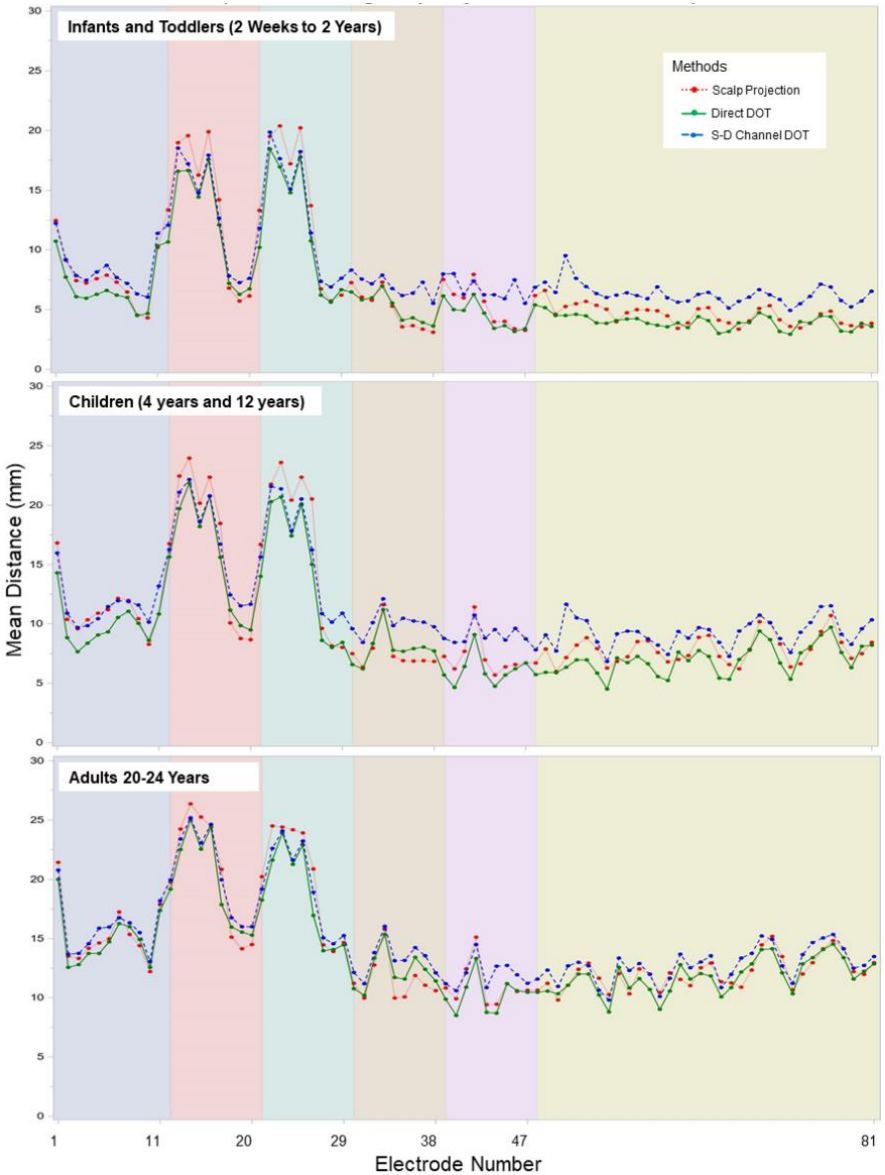
Infants and Toddlers (2 Weeks to 2 Years)
Children (4 years and 12 years)
Adults 20-24 Years
Methods
Scalp Projection
Direct DOT
S-D Channel DOT
Mean Distance (mm)
Electrode Number
1
11
20
29
38
47
81

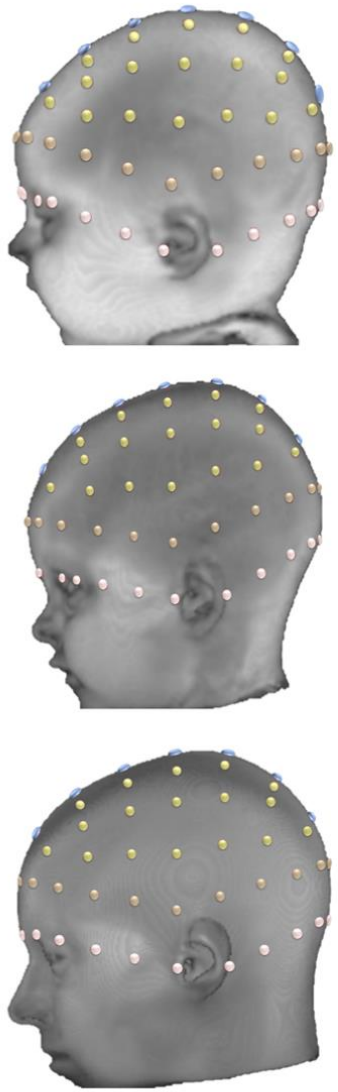

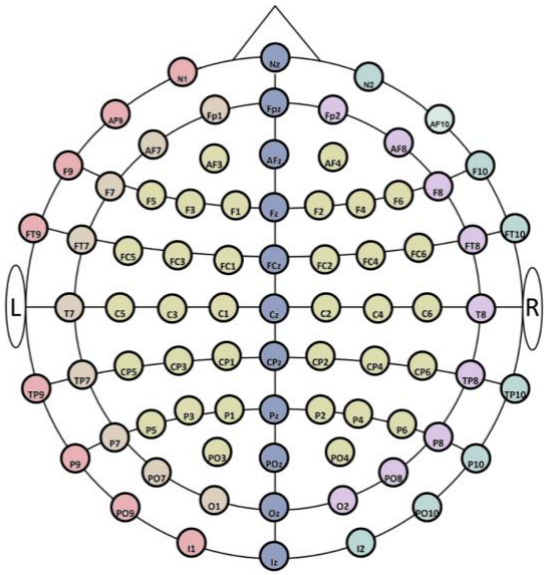
L
R

B.

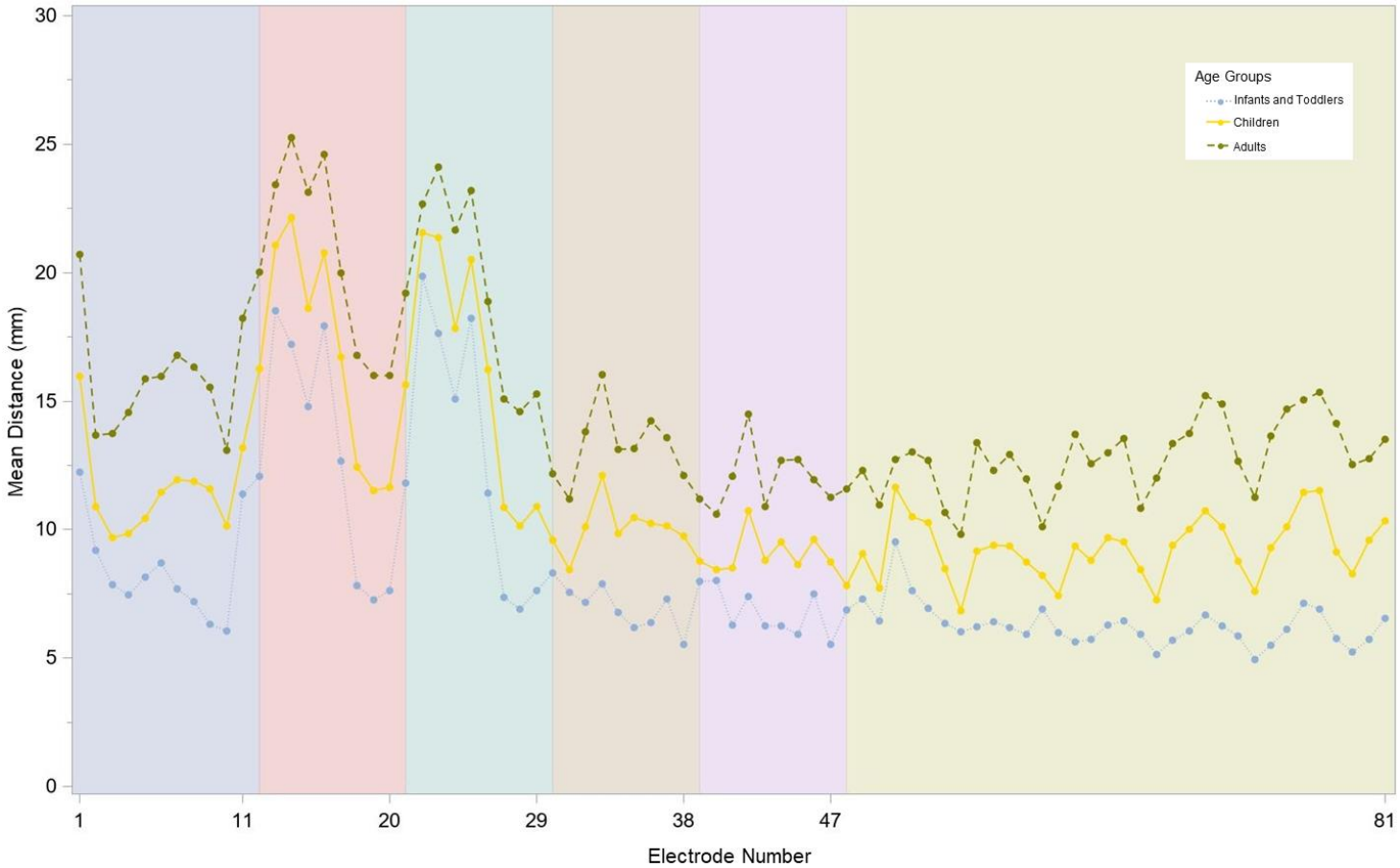

Fig 6. Mean scalp-to-cortex distances across 10-10 electrode and channel locations by age groups. A. Distances estimated using Scalp Projection, Direct DOT and S-D Channel DOT with individual MRIs. Electrodes were divided into five groups. In addition, a two-dimensional layout of the 10-10 system (top right), a three-dimensional rendering of the electrode locations on a 3-month-old infant average template (top left), a 4-year-old child average template (middle) and a 20-24-year-old adult average template (bottom) were displayed to aid visualization. The 10-10 electrode name and the number in the figure are in Table 3, and the five electrode groups are listed in Figure 1. B. Mean S-D Channel DOT distances for infants and toddlers (2 weeks to 2 years), Children (4 years and 12 years) and adults (20-24 years).

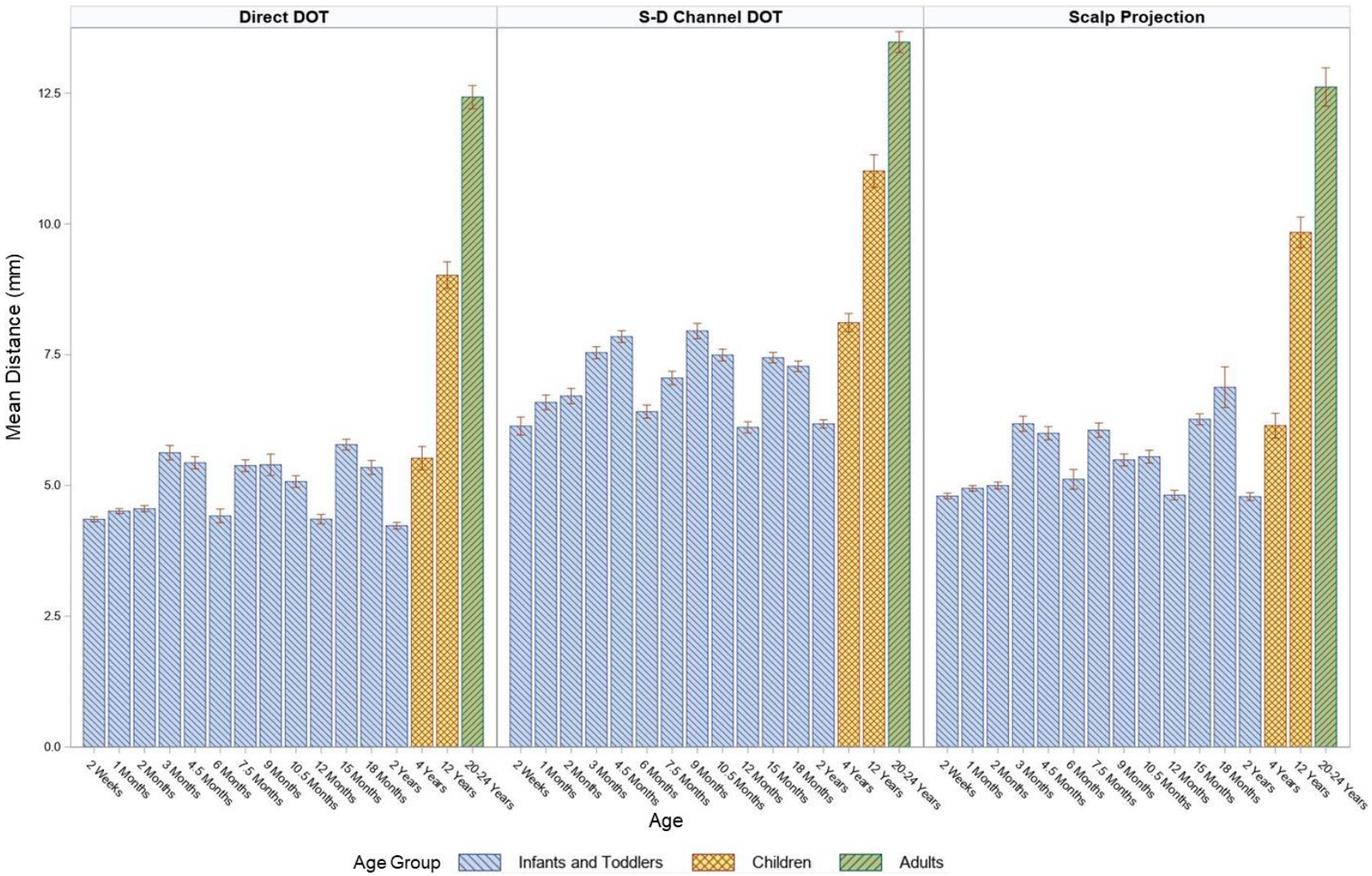

Fig 7. Mean scalp-to-cortex distances by age groups (data for electrodes N1, AF9, F9, FT9, T9/LPA, TP9, N2, AF10, F10, FT10, T10/RPA, and TP10 were excluded). The distances were estimated using scalp projection, Direct DOT and S-D Channel DOT with individual MRI.

three estimation methods, excluding the frontal-central bottom row electrodes. The differences in the distances for the infant ages did not show a systematic age-related change. The Scalp Projection and Direct DOT distances were similar, and the S-D Channel DOT distances were larger than the distances from the other methods. We also tested whether scalp-to-cortex distances changed significantly from infancy (2 weeks to 2 years) to childhood (4 years and 12 years) and to adulthood (20-24 years). Results from the one-way ANOVAs confirmed the age group effect in distances estimated using scalp projection, F (2, 975) = 508.61, $p < .001$, Direct DOT, F (2, 1054) = 1721.08, $p < .001$, and S-D Channel DOT, F (2, 1054) = 1267.73, $p < .001$ (c.f. Figure 6B). Post-hoc analyses using Tukey's test showed that the distances increased from infancy and toddlerhood to childhood and from childhood to adulthood for all estimation methods, all p's < .05. Figure 7 shows an obvious change from the infant to the child/adolescent and adult ages in scalp-to-cortex distance.

The scalp-to-cortex distances were examined also for the average MRI templates. Supplemental Figure 4 shows the S-D Channel DOT distance across age for the distances calculated from the average MRI templates. The distances for the participant-based averages (e.g., Figure 6B, Figure 7) were similar to the distances calculated from the average MRI template (Supplemental Information Figure 4).

Scalp-location-to-ROI Mapping

The Scalp Projection and the S-D Channel DOT sensitivity were used to generate look-up tables that show the cortical ROIs for each of the 10-10 electrodes. An Excel spreadsheet is presented in the Supplementary Information with this information (Supplemental Information: Table3_TenTen_CombinedDistributionFile_AllAges_SP_MCXSD.xlsx). This table has a tab for each estimation type and age combination (e.g., Spatial 2-0 Weeks, Spatial 1-0Month, Source-

Detector-DOT 2-0Weeks, Source-Detector-DOT 1-Month….). Each table has one row for each electrode containing columns for the electrode name and the cortical ROIs for the lobar, Hammers, and LPBA40 atlases. This table could be used to find a specific electrode-ROI combination for each of the ages in the study. We use the name "electrode" and "channel" interchangeably, though the "electrode location" properly refers to the Scalp Projection method where the "channel location" properly refers to the S-D Channel DOT method.

The Scalp Projection and S-D Channel DOT estimations yielded overlapping and considerably different scalp-location-to-ROI Mappings. For example, between-method discrepancy was found at 32 scalp locations where the electrode was mapped to at least one different ROI for the 3-month group. The discrepancy was found at 29 scalp locations for the 20-24-year-olds.

Table 3 summarizes the age differences in S-D Channel DOT sensitivity to atlas ROIs at each 10-10 channel location. The channel-location-to-ROI correspondences showed stability over age for some of the electrode/atlas ROIs. The lobar atlas has macrostructural segmentations which resulted in similar channel-to-ROI correspondence across ages. Most of the channel locations (52 out of 81 channels) were mapped to one lobar atlas ROI for all age groups. Some channels were sensitive to more than one lobar ROIs in younger age groups but were mapped to one lobar ROI in older age groups (CZ, PZ, OZ, F9, F10, T10, FT7, FT8, O1, O2, C5, C6, C1, C2, CP5, and CP6). For example, O1 (left) and O2 (right) were mapped to the cerebellum, fusiform gyrus, occipital lobe, and parietal lobe for the infant groups but only to the occipital lobe for 20-24-year-olds. Some channels were sensitive to more than one lobar ROIs only in older age groups (POZ, PO9, I1, and I2). For example, I2 corresponded to both the right cerebellum and occipital lobe in 12- and 20-24-year-olds but only to the cerebellum in younger

Table 3. Atlas locations corresponding to the scalp channel locations. For each channel location, we listed atlas region of interest (ROI) that had at least 25% of its voxels intersected with the 1.5cm-radius sphere created around the channel location. We also listed the age groups with the ROI that survived the threshold.

Electrode Number	Electrode Name	Lobar Atlas ROI	Ages	Hammer Atlas ROI	Ages	LPBA40 Atlas ROI	Ages
1	NZ	Frontal	All	Medial orbital gyrus	All	Superior frontal gyrus	All
				Superior frontal gyrus	2ws to 4.5ms, 20-24yrs		
2	FPZ	Frontal	All	Superior frontal gyrus	All	Middle frontal gyrus	2ms
						Superior frontal gyrus	All
3	AFZ	Frontal	All	Superior frontal gyrus	All	Superior frontal gyrus	All
4	FZ	Frontal	All	Superior frontal gyrus	All	Superior frontal gyrus	All
5	FCZ	Frontal	All	Superior frontal gyrus	All	Superior frontal gyrus	All
6	CZ	Frontal	All	Postcentral gyrus	1m	Precentral gyrus	2ws to 4.5ms; 7.5ms to 20-24yrs
		Parietal	2ws to 2ms	Precentral gyrus	All	Superior frontal gyrus	2ms to 20-24yrs
				Superior frontal gyrus	3ms to 12ms, 18ms to 20-24yrs		
				Superior parietal gyrus	2ws		
7	CPZ	Parietal	All	Postcentral gyrus	6ms, 12yrs, 20-24yrs	Postcentral gyrus	3ms to 20-24yrs
				Superior parietal gyrus	All	Precuneus	2ws to 3ms; 15ms
						Superior parietal gyrus	All
8	PZ	Occipital	2ws, 1m	Cuneus	2ws, 1m	Precuneus	2ms to 20-24yrs
		Parietal	All	Superior parietal gyrus	All	Superior parietal gyrus	1ms to 20-24yrs
9	POZ	Occipital	All	Cuneus	All	Cuneus	All
		Parietal	20-24yrs	Lateral remainder of occipital lobe	2ws to 2ms, 7.5ms, 12ms,	Superior occipital gyrus	2ms to 20-24yrs
				Superior parietal gyrus	12yrs		
10	OZ	Fusiform	2ws, 1m, 3ms, 4.5ms, 9ms, 10.5ms, 15ms, 18ms	Cuneus	2ms to 20-24yrs	Cuneus	3ms to 20-24yrs
		Occipital	All	Lateral remainder of occipital lobe	All	Lingual gyrus	1m, 3ms, 4.5ms
				Lingual gyrus	2ws, 1m, 3ms, 4.5ms	Middle occipital gyrus	2ms, 4.5ms to 4yrs, 20-24yrs
11	IZ	Cerebellum	2ws to 4yrs	Cerebellum	2ws to 12yrs	Cerebellum	2ws to 12yrs

		Fusiform	10.5ms, 2yrs, 4yrs, 20-24yrs	Lateral remainder of occipital lobe	12yrs, 20-24yrs	Lingual gyrus	12yrs, 20-24yrs
		Occipital	12yrs, 20-24yrs	Lingual gyrus	12yrs, 20-24yrs		
12	N1	Frontal	All	Anterior orbital gyrus	All	Middle frontal gyrus	2ws to 2ms
				Medial orbital gyrus	All	Middle orbitofrontal gyrus	4.5ms to 20-24yrs
				Superior frontal gyrus	2ws, 1m	Superior frontal gyrus	All
13	AF9	Frontal	All	Anterior orbital gyrus	2ws to 9ms, 12ms, 2yrs, 4yrs	Lateral orbitofrontal gyrus	4.5ms, 10.5ms, 15ms, 2yrs to 20-24yrs
				Lateral orbital gyrus	4.5ms, 10.5ms, 15ms, 2yrs to 20-24yrs	Middle orbitofrontal gyrus	3ms to 12ms, 18ms to 4yrs
				Medial orbital gyrus	12ms		
14	F9	Frontal	2ws to 3ms	Anterior temporal lobe, lateral part	4.5ms to 20-24yrs	Middle temporal gyrus	10.5ms, 15ms, 20-24yrs
		Temporal	All	Anterior temporal lobe, medial part	12ms, 18ms, 2yrs, 4yrs	Superior temporal gyrus	All
				Superior temporal gyrus, anterior part	9ms, 10.5ms, 15ms, 12yrs, 20-24yrs		
15	FT9	Temporal	All	Anterior temporal lobe, lateral part	3ms to 20-24yrs	Inferior temporal gyrus	All
				Medial and inferior temporal gyri	All	Middle temporal gyrus	1m to 20-24yrs
						Superior temporal gyrus	2ws to 3ms
16	T9	Temporal	All	Medial and inferior temporal gyri	All	Inferior temporal gyrus	All
						Middle temporal gyrus	2ws to 3ms, 20-24yrs
17	TP9	Cerebellum	All	Cerebellum	All	Cerebellum	All
18	P9	Cerebellum	All	Cerebellum	All	Cerebellum	All
19	PO9	Cerebellum	All	Cerebellum	All	Cerebellum	All
		Parietal	12yrs, 20-24yrs	Lateral remainder of occipital lobe	12yrs, 20-24yrs	Inferior occipital gyrus	12yrs, 20-24yrs
20	I1	Cerebellum	All	Cerebellum	All	Cerebellum	All
		Occipital	12yrs, 20-24yrs	Lateral remainder of occipital lobe	6ms, 12yrs, 20-24yrs	Inferior occipital gyrus	6ms, 10.5ms, 12yrs, 20-24yrs
		Parietal	12yrs				
21	N2	Frontal	All	Anterior orbital gyrus	3ms, 6ms, 7.5ms, 12yrs, 20-24yrs	Middle orbitofrontal gyrus	6ms, 7.5ms, 2yrs to 20-24yrs
				Medial orbital gyrus	All	Superior frontal gyrus	All
				Superior frontal gyrus	2ws to 2ms		

22	AF10	Frontal	All	Anterior orbital gyrus	All	Lateral orbitofrontal gyrus	12yrs, 20-24yrs
				Lateral orbital gyrus	12yrs, 20-24yrs	Middle frontal gyrus	2ws, 1m
				Medial orbital gyrus	7.5ms to 12ms, 18ms, 2yrs	Middle orbitofrontal gyrus	1m to 12yrs
						Superior frontal gyrus	12ms
23	F10	Frontal	2ws to 7.5ms	Anterior temporal lobe, lateral part	9ms, 10.5ms, 15ms, 2yrs 12yrs, 20-24yrs	Middle temporal gyrus	20-24yrs
		Temporal	All	Anterior temporal lobe, medial part	4.5ms to 4yrs	Superior temporal gyrus	All
				Superior temporal gyrus, anterior part	9ms, 15ms, 18ms, 4yrs to 20-24yrs		
24	FT10	Temporal	All	Anterior temporal lobe, lateral part	3ms to 20-24yrs	Inferior temporal gyrus	All
				Anterior temporal lobe, medial part	1m, 2ms, 7.5ms, 12ms	Middle temporal gyrus	3ms to 20-24yrs
				Medial and inferior temporal gyri	6ms, 9ms, 10.5ms, 15ms 2yrs, 12yrs, 20-24yrs	Superior temporal gyrus	1m to 3ms, 6ms, 7.5ms
25	T10	Cerebellum	10.5ms, 15ms	Cerebellum	10.5ms, 15ms	Cerebellum	10.5ms, 15ms
		Temporal	All	Medial and inferior temporal gyri	All	Inferior temporal gyrus	All
						Middle temporal gyrus	2ws to 3ms, 6ms, 20-24yrs
26	TP10	Cerebellum	All	Cerebellum	All	Cerebellum	All
27	P10	Cerebellum	All	Cerebellum	All	Cerebellum	All
28	PO10	Cerebellum	All	Cerebellum	All	Cerebellum	All
				Lateral remainder of occipital lobe	12yrs, 20-24yrs	Inferior occipital gyrus	12yrs, 20-24yrs
29	I2	Cerebellum	All	Cerebellum	All	Cerebellum	All
		Occipital	12yrs, 20-24yrs	Lateral remainder of occipital lobe	6ms, 7.5ms, 2yrs to 20-24yrs	Inferior occipital gyrus	6ms, 10.5ms, 2yrs to 20-24yrs
						Middle occipital gyrus	20-24yrs
30	FP1	Frontal	All	Anterior orbital gyrus	2yrs	Middle frontal gyrus	All
				Middle frontal gyrus	All		
				Superior frontal gyrus	2ws to 2yrs, 12yrs, 20-24yrs		
31	AF7	Frontal	All	Lateral orbital gyrus	7.5ms, 2yrs, 4yrs	Inferior frontal gyrus	All
				Middle frontal gyrus	All	Middle frontal gyrus	2ws to 10.5ms, 18ms
32	F7	Frontal	All	Inferior frontal gyrus	All	Inferior frontal gyrus	All

				Lateral orbital gyrus	6ms, 7.5ms, 2yrs	Lateral orbitofrontal gyrus	4.5ms, 6ms, 9ms to 12yrs
33	FT7	Frontal	2ws to 3ms	Medial and inferior temporal gyri	4yrs	Middle temporal gyrus	All
		Temporal	All	Superior temporal gyrus, anterior part	3ms to 20-24yrs	Superior temporal gyrus	All
34	T7	Temporal	All	Medial and inferior temporal gyri	All	Inferior temporal gyrus	4.5ms
				Superior temporal gyrus, central part	2ms	Middle temporal gyrus	All
						Superior temporal gyrus	2ws to 3ms, 10.5ms
35	TP7	Temporal	All	Medial and inferior temporal gyri	2ws, 3ms	Inferior temporal gyrus	2ws to 12yrs
				Posterior temporal lobe	All	Middle temporal gyrus	All
36	P7	Cerebellum	2ws, 1m	Cerebellum	2ws, 1m	Cerebellum	2ws, 1m
		Parietal	6ms, 2yrs, 12yrs, 20-24yrs	Lateral remainder of occipital lobe	6ms to 10.5ms, 15ms to 4yrs	Inferior temporal gyrus	4.5ms to 7.5ms, 12ms, 18ms to 4yrs
		Temporal	All	Posterior temporal lobe	All	Middle occipital gyrus	10.5ms to 15ms, 2yrs, 20-24yrs
						Middle temporal gyrus	6ms, 12ms, 12yrs, 20-24yrs
37	PO7	Cerebellum	2ws to 2ms, 4.5ms	Cerebellum	2ws, 1m	Cerebellum	2ws, 1m
		Fusiform	10.5ms, 15ms	Lateral remainder of occipital lobe	All	Inferior occipital gyrus	2ws to 4yrs
		Occipital	6ms, 12ms, 2yrs, 4yrs			Middle occipital gyrus	2ms to 20-24yrs
		Parietal	2m to 20-24yrs				
38	O1	Cerebellum	2ws, 1m,	Cerebellum	2ws	Cerebellum	2ws
		Fusiform	4.5ms, 9ms, 15ms, 18ms	Lateral remainder of occipital lobe	All	Inferior occipital gyrus	2ws, 1m, 4.5ms
		Occipital	1m to 20-24yrs			Middle occipital gyrus	All
		Parietal	3ms, 4.5ms, 7.5ms, 18ms, 12yrs				
39	FP2	Frontal	All	Anterior orbital gyrus	7.5ms, 2yrs	Middle frontal gyrus	All
				Middle frontal gyrus	All	Superior frontal gyrus	1m, 2ms
				Superior frontal gyrus	All		
40	AF8	Frontal	All	Anterior orbital gyrus	6ms to 12ms, 18ms, 2yrs	Inferior frontal gyrus	All
				Middle frontal gyrus	All	Middle frontal gyrus	2ws to 12yrs
41	F8	Frontal	All	Inferior frontal gyrus	All	Inferior frontal gyrus	All
				Lateral orbital gyrus	4.5ms to 4yrs	Lateral orbitofrontal gyrus	3ms to 12yrs

							3ms, 4.5ms, 9ms, 10.5ms, 15ms, 12yrs,
42	FT8	Frontal	2ws to 2ms, 6ms	Medial and inferior temporal gyri	20-24yrs	Middle temporal gyrus	20-24yrs
		Temporal	All	Superior temporal gyrus, anterior part	3ms to 20-24yrs	Superior temporal gyrus	All
43	T8	Temporal	All	Medial and inferior temporal gyri	All	Inferior temporal gyrus	10.5ms
						Middle temporal gyrus	All
						Superior temporal gyrus	2ws to 2ms, 6ms, 7.5ms, 4yrs
44	TP8	Temporal	All	Medial and inferior temporal gyri	2ms to 7.5ms	Inferior temporal gyrus	All
				Posterior temporal lobe	All	Middle temporal gyrus	All
45	P8	Cerebellum	2ws to 2ms	Cerebellum	2ws, 1m	Cerebellum	2ws, 1m
		Fusiform	15ms	Lateral remainder of occipital lobe	10.5ms, 15ms, 18ms, 20-24yrs	Inferior temporal gyrus	6ms to 12ms, 18ms to 4yrs
		Parietal	6ms, 4yrs to 20-24yrs	Posterior temporal lobe	All	Middle occipital gyrus	20-24yrs
		Temporal	All			Middle temporal gyrus	2ms, 6ms to 12ms, 18ms to 20-24yrs
46	PO8	Cerebellum	2ws to 2ms	Cerebellum	2ws, 1m	Cerebellum	2ws, 1m
		Fusiform	9ms, 10.5ms, 15ms, 18ms	Lateral remainder of occipital lobe	All	Inferior occipital gyrus	2ws to 2yrs
		Occipital	12ms, 2yrs, 4yrs, 12-24yrs			Middle occipital gyrus	1m to 20-24yrs
		Parietal	3ms to 12ms, 18ms to 20-24yrs				
47	O2	Cerebellum	2ws to 2ms	Lateral remainder of occipital lobe	All	Inferior occipital gyrus	2ws, 1m, 4.5ms
		Fusiform	9ms, 10.5ms, 15ms, 18ms			Middle occipital gyrus	All
		Occipital	All				
		Parietal	3ms, 4.5ms, 7.5ms				
48	AF3	Frontal	All	Middle frontal gyrus	All	Middle frontal gyrus	All
				Superior frontal gyrus	All		
49	AF4	Frontal	All	Middle frontal gyrus	All	Middle frontal gyrus	All
				Superior frontal gyrus	All	Superior frontal gyrus	2ws to 2ms, 6ms
50	F5	Frontal	All	Inferior frontal gyrus	All	Inferior frontal gyrus	All
				Middle frontal gyrus	All	Middle frontal gyrus	All

51	F3	Frontal	All	Middle frontal gyrus	All	Inferior frontal gyrus	2ws, 4.5ms to 12ms, 4yrs
						Middle frontal gyrus	All
52	F1	Frontal	All	Middle frontal gyrus	2ws to 12yrs	Middle frontal gyrus	All
				Superior frontal gyrus	All	Superior frontal gyrus	2ws to 4.5ms, 7.5ms to 2yrs, 12yrs, 20-24yrs
53	F2	Frontal	All	Middle frontal gyrus	2ws to 4yrs	Middle frontal gyrus	All
				Superior frontal gyrus	All	Superior frontal gyrus	All
54	F4	Frontal	All	Middle frontal gyrus	All	Middle frontal gyrus	All
55	F6	Frontal	All	Inferior frontal gyrus	All	Inferior frontal gyrus	All
				Middle frontal gyrus	All	Middle frontal gyrus	All
56	FC5	Frontal	All	Inferior frontal gyrus	All	Inferior frontal gyrus	All
				Precentral gyrus	All	Precentral gyrus	All
57	FC3	Frontal	All	Middle frontal gyrus	All	Middle frontal gyrus	All
				Precentral gyrus	2ws to 4yrs	Precentral gyrus	2ws to 12yrs
58	FC1	Frontal	All	Middle frontal gyrus	2ws, 2ms to 20-24yrs	Middle frontal gyrus	All
				Precentral gyrus	2ws, 1m	Precentral gyrus	2ws, 1m
				Superior frontal gyrus	All	Superior frontal gyrus	All
59	FC2	Frontal	All	Middle frontal gyrus	1ms to 20-24yrs	Middle frontal gyrus	1m to 20-24yrs
				Precentral gyrus	2ws	Superior frontal gyrus	All
				Superior frontal gyrus	All		
60	FC4	Frontal	All	Middle frontal gyrus	All	Middle frontal gyrus	All
				Precentral gyrus	2ws to 2ms, 10.5ms, 12ms, 15ms	Precentral gyrus	2ws to 2ms, 9ms, 12ms, 15ms, 12yrs
61	FC6	Frontal	All	Inferior frontal gyrus	All	Inferior frontal gyrus	All
				Precentral gyrus	2ws to 2ms, 9ms to 20-24yrs	Precentral gyrus	2ws to 2ms, 9ms to 20-24yrs
62	C5	Parietal	All	Postcentral gyrus	3ms to 20-24yrs	Postcentral gyrus	4.5ms to 20-24yrs
		Temporal	2ws to 4yrs	Remainder of parietal lobe (including supramarginal and angular gyrus)	1ms, 10.5ms, 15ms, 2yrs 4yrs, 20-24yrs	Superior temporal gyrus	2ws to 4yrs
				Superior temporal gyrus, central part	3ms to 9ms, 12ms to 4yr	Supramarginal gyrus	15ms, 20-24yrs

63	C3	Frontal	3ms, 6ms to 10.6ms, 18ms, 12yrs, 20-24yrs	Postcentral gyrus	All	Postcentral gyrus	All
		Parietal	All	Precentral gyrus	3ms, 6ms, 7.5ms, 12yrs	Precentral gyrus	3ms to 10.5ms, 12yrs
				Remainder of parietal lobe (including supramarginal and angular gyrus)	2ws to 4yrs, 20-24yrs	Supramarginal gyrus	2ws to 4.5ms, 7.5ms, 9ms, 12ms to 4yrs
64	C1	Frontal	All	Postcentral gyrus	2ws to 4.5ms, 7.5ms to 4yrs	Postcentral gyrus	2ws to 2ms, 7.5ms, 12ms to 4yrs
		Parietal	2ws to 4yrs	Precentral gyrus	All	Precentral gyrus	All
				Superior parietal gyrus	1m	Superior parietal gyrus	1m
65	C2	Frontal	All	Postcentral gyrus	2ws to 2ms, 12ms, 15ms	Postcentral gyrus	2ws, 1m, 15ms
		Parietal	2ws to 3ms, 12ms, 15ms	Precentral gyrus	All	Precentral gyrus	All
						Superior frontal gyrus	4.5ms, 6ms, 9ms
						Superior parietal gyrus	2ws
66	C4	Frontal	2ws, 2ms to 20-24yrs	Postcentral gyrus	All	Postcentral gyrus	All
		Parietal	All	Precentral gyrus	3ms to 10.5ms, 18ms to 20-24yrs	Precentral gyrus	2ms to 20-24yrs
				Remainder of parietal lobe (including supramarginal and angular gyrus)	2ws to 2ms, 15ms	Supramarginal gyrus	2ws to 2ms
67	C6	Parietal	All	Postcentral gyrus	2ms to 20-24yrs	Postcentral gyrus	3ms to 20-24yrs
		Temporal	2ws to 12yrs	Remainder of parietal lobe (including supramarginal and angular gyrus)	12yrs, 20-24yrs	Superior temporal gyrus	2ws to 2yrs, 20-24yrs
				Superior temporal gyrus, central part	1ms to 2yrs	Supramarginal gyrus	20-24yrs
68	CP5	Parietal	All	Posterior temporal lobe	All	Angular gyrus	4.5ms, 9ms to 20-24yrs
		Temporal	2ws to 12yrs	Remainder of parietal lobe (including supramarginal and angular gyrus)	All	Middle temporal gyrus	2ws to 2ms, 4yrs
						Superior temporal gyrus	6ms, 7.5ms, 12ms, 18ms to 4yrs
						Supramarginal gyrus	6ms, 7.5ms, 10.5ms, 12ms, 18ms, 12yrs, 20-24yrs
69	CP3	Parietal	All	Remainder of parietal lobe (including supramarginal and angular gyrus)	All	Angular gyrus	All
						Supramarginal gyrus	2ms to 20-24yrs

70	CP1	Parietal	All	Remainder of parietal lobe (including supramarginal and angular gyrus)	2ws	Postcentral gyrus	10.5ms, 20-24yrs
				Superior parietal gyrus	All	Superior parietal gyrus	All
71	CP2	Parietal	All	Postcentral gyrus	6ms	Postcentral gyrus	6m
				Remainder of parietal lobe (including supramarginal and angular gyrus)	1m	Superior parietal gyrus	All
				Superior parietal gyrus	All		
72	CP4	Parietal	All	Remainder of parietal lobe (including supramarginal and angular gyrus)	All	Angular gyrus	2ws to 4.5ms, 7.5ms to 20-24yrs
						Supramarginal gyrus	1m to 20-24yrs
73	CP6	Parietal	All	Posterior temporal lobe	2ws to 12yrs	Middle temporal gyrus	2ws, 1m
		Temporal	2ws to 12yrs	Remainder of parietal lobe (including supramarginal and angular gyrus)	All	Superior temporal gyrus	2ws to 12yrs
						Supramarginal gyrus	2ms to 20-24yrs
74	P5	Parietal	All	Lateral remainder of occipital lobe	2ws to 4yrs, 20-24yrs	Angular gyrus	2ms to 20-24yrs
				Posterior temporal lobe	2ws to 7.5ms, 12ms, 18ms, 4yrs	Middle occipital gyrus	All
				Remainder of parietal lobe (including supramarginal and angular gyrus)	2ms to 20-24yrs		
75	P3	Parietal	All	Lateral remainder of occipital lobe	2ws to 4yrs	Angular gyrus	2ms to 20-24yrs
				Remainder of parietal lobe (including supramarginal and angular gyrus)	2ms to 20-24yrs	Middle occipital gyrus	2ws to 9ms, 12ms to 4yrs.
76	P1	Parietal	All	Lateral remainder of occipital lobe	2ws to 4.5ms, 9ms, 12ms, 15ms, 4yrs	Middle occipital gyrus	2ws, 1m
				Superior parietal gyrus	2ms to 20-24yrs	Superior occipital gyrus	2ws, 1m
						Superior parietal gyrus	2ms to 20-24yrs
77	P2	Parietal	All	Lateral remainder of occipital lobe	2ws to 4.5ms, 9ms, 12ms, 15ms	Angular gyrus	12ms, 2yrs
				Remainder of parietal lobe (including supramarginal and angular gyrus)	2yrs	Middle occipital gyrus	2ws, 1m
				Superior parietal gyrus	2ws, 2ms to 20-24yrs	Superior occipital gyrus	2ws, 1m
						Superior parietal gyrus	2ms to 20-24yrs
78	P4	Parietal	All	Lateral remainder of occipital lobe	2ws to 4.5ms, 9ms to 18ms	Angular gyrus	All
				Remainder of parietal lobe (including supramarginal and angular gyrus)	All	Middle occipital gyrus	2ws to 3ms, 15ms

79	P6	Parietal	All	Lateral remainder of occipital lobe	2ws to 4.5ms, 9ms to 4yrs, 20-24yrs	Angular gyrus	2ms to 20-24yrs
				Posterior temporal lobe	2ws to 7.5ms, 10.5ms to 2yrs	Middle occipital gyrus	2ws to 4.5ms, 7.5ms to 4yrs
				Remainder of parietal lobe (including supramarginal and angular gyrus)	2ms to 20-24yrs		
80	PO3	Occipital	All	Lateral remainder of occipital lobe	All	Middle occipital gyrus	All
		Parietal	2ms to 20-24yrs			Superior occipital gyrus	2ms to 20-24yrs
81	PO4	Cerebellum	2ws, 2ms	Lateral remainder of occipital lobe	All	Middle occipital gyrus	All
		Occipital	All			Superior occipital gyrus	4.5ms to 7.5ms, 10.5ms, 15ms, 18ms, 4yrs to 20-24yrs
		Parietal	2ms to 20-24yrs				

ages. Other channels had similar channel-to-ROI mappings over age (IZ, P7, P8, PO7, PO8, C3, C4, PO3, and PO4).

The Hammers and LPBA40 atlases have smaller structural segmentations than the lobar atlas. Hence, most of the channel locations were mapped to more than one ROI. At 44 channel locations, at least one identical ROI from the Hammers and LPBA40 atlas was mapped to the channel locations across all age groups. There were channels that were sensitive to superior frontal gyrus (FPZ, AFZ, FZ, FCZ, F2, FC1, and FC2), middle frontal gyrus (FP1, FP2, AF3, AF4, F5, F3, F4, F6, FC3, and FC4), inferior frontal gyrus (F7, F8, F5, F6, FC5, and FC6), precentral gyrus (FC5, C1, and C2), postcentral gyrus (C3 and C4), superior parietal gyrus (CPZ, CP1, and CP2), angular gyrus (CP3 and P4), cuneus (POZ), inferior temporal gyrus (FT9, T9, and T10), middle temporal gyrus (T7 and T8), and cerebellum (TP9, P9, PO9, I1, TP10, P10, PO10, and I2) across all age groups. However, many channel locations displayed variations in the channel-to-ROI mapping across age groups. There tended to be less channel specificity to ROI locations in younger groups. For example, the C1 was mapped to both postcentral and precentral gyrus from the ages of 2 weeks to 4 years whereas it corresponded to only precentral gyrus in older age groups.

Depth Sensitivity Profiles by Source-Detector Separation Distances

We examined the S-D Channel DOT fluence as a function of penetration depths (PPL) sampled in the fluence distribution. This was done by selecting 10-5 location pairs with separation distances from 10 mm to 60 mm by 5 mm increments and calculating the S-D Channel DOT fluence for each pair and averaging over pairs of the same distance. Figure 8 displays examples of the depth sensitivity profiles plotted by channels (separate lines) and separation distances (panels) for one individual from four different ages at 20 mm and 50 mm

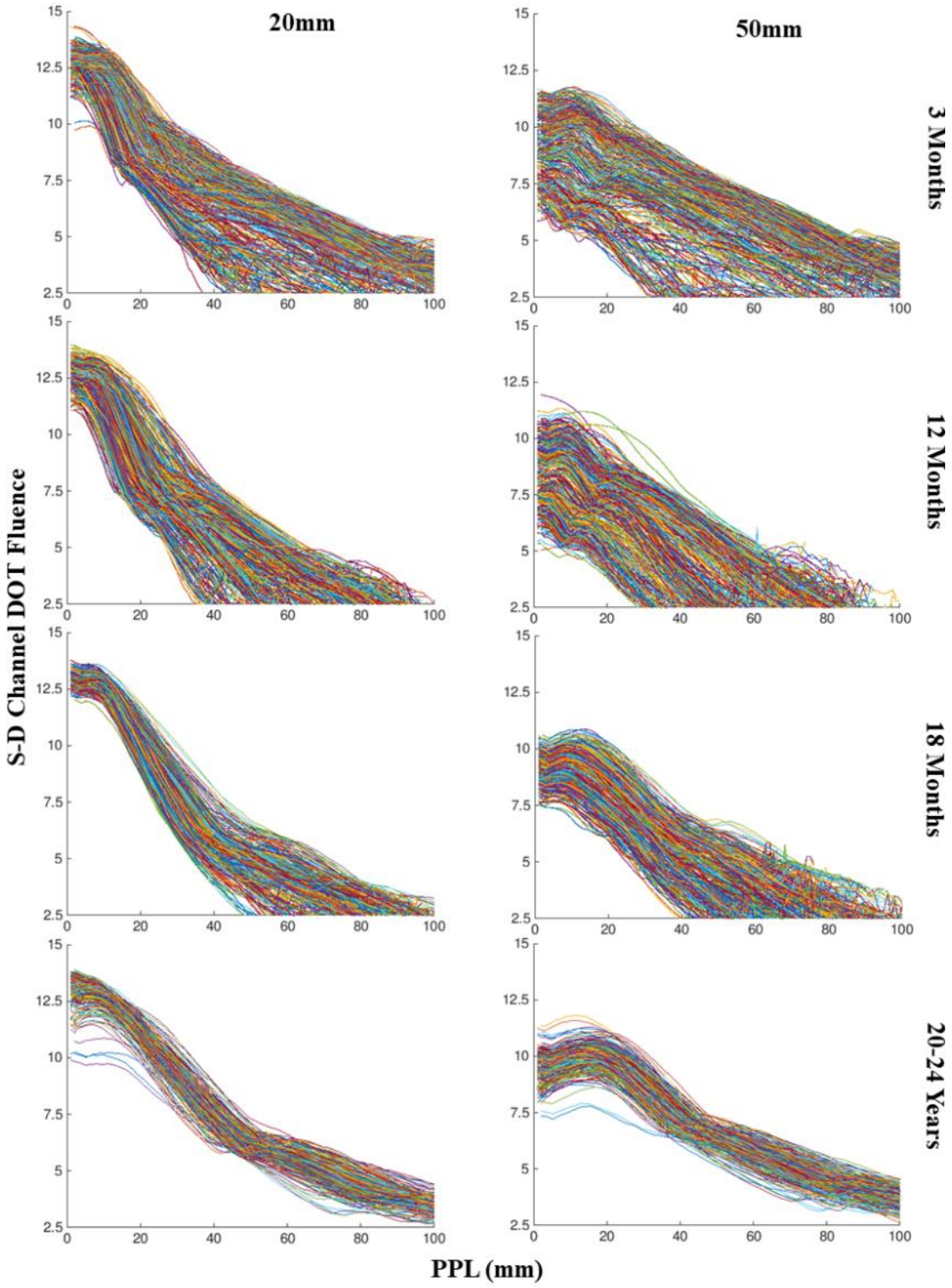

Fig 8. Source-Detector (S-D) Channel DOT fluence sensitivity profile by channels. Four example individuals were selected, one from each age category. The S-D Channel DOT fluence value was plotted as a function of the partial path length (PPL) separately for channels at the source-detector separations for 20 mm and 50 mm for each individual.

separations (more examples are displayed in Supplemental Information Figures 9A and 9B). The sensitivity profiles across the four individuals showed greater peaks and steeper slopes for channels at 20 mm than 50 mm separation. The between-channel variance showed a systematic decline from the infants to the adults. The variance increased from 20 mm to 50 mm separations for the infant groups whereas it remained stable for the adult group.

The sensitivity profiles changed with separation distances across age groups. Figure 9A shows the S-D Channel DOT fluence as a function of partial path length (PPL) separately for the target source-detector distances, averaged across channel locations, and separately for four age bins. We grouped the samples to four age bins for averages for some analyses based on preliminary data visualization: 2 weeks through 4.5 months; 6 months through 12 months; 15 months through 2 years; 4, 12, and 20-24 years. The sensitivity profile changed systematically with the source-detector distance. The peak of the sensitivity function was largest at the smallest separation distance and decreased as source-detector distance increased. However, the fluence value dissipated more quickly at the shorter source-detector distances than the longer distances, with the distributions becoming flatter across increasing source-detector distance. Compared to the sensitivity profile at shorter separation distances, the same fluence value was carried to greater penetration depth at larger separation.

The patterns of age-related differences in the sensitivity profiles were relatively consistent across separation distances. Figures 9B, 9C, and 9D show the S-D Channel DOT fluence sensitivity functions for the 20 mm, 30 mm, and 50 mm source-detector separations, respectively, and separately for the testing ages. There were consistent age changes in the shape of the sensitivity function over the source-detector separations. These are most easily seen in the profile for the 50 mm separation (Figure 9D). The 2-week through 4.5 month old age groups

A.

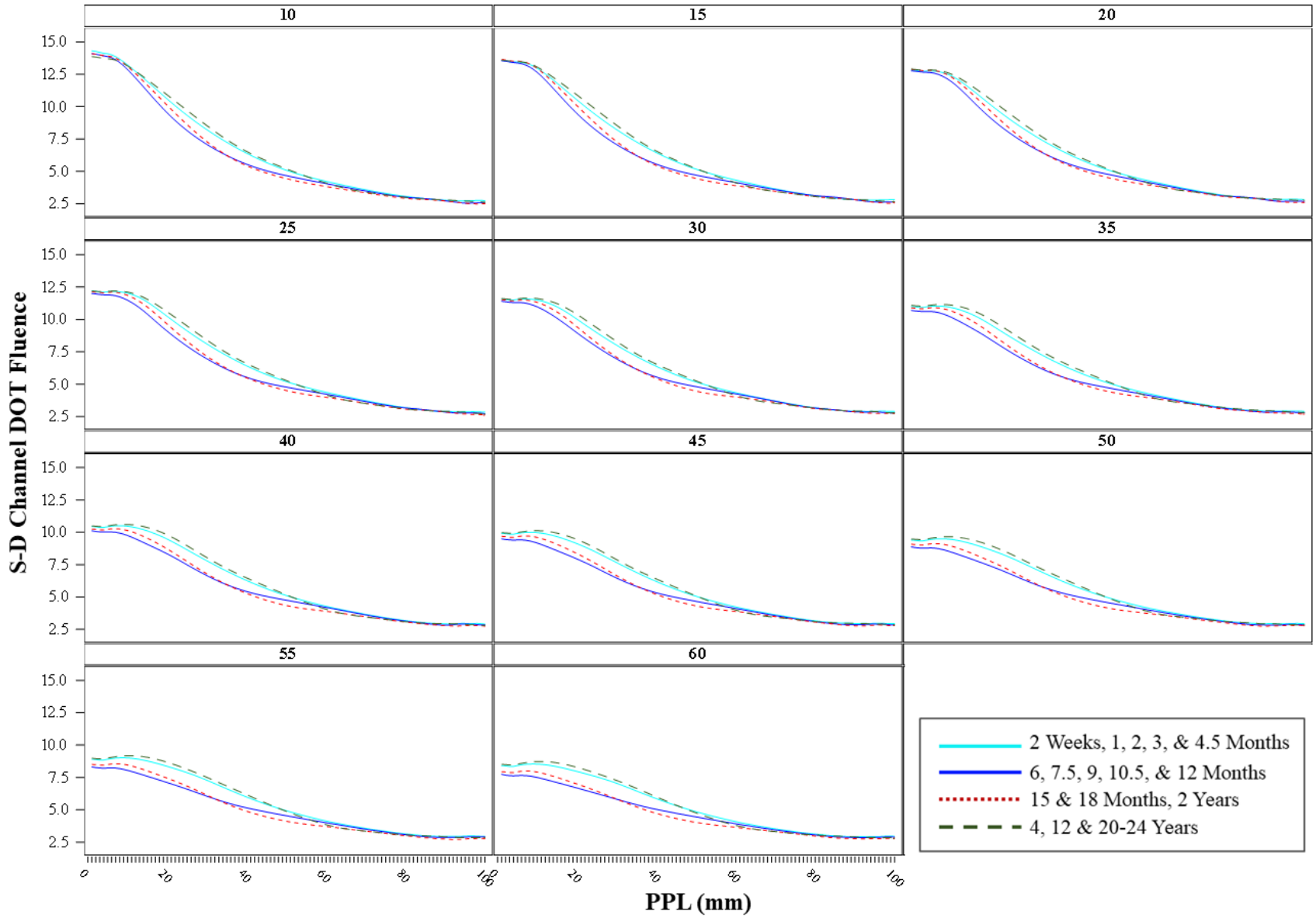
10
15
20
25
30
35
40
45
50
55
60
15.0
12.5
10.0
7.5
5.0
2.5
S-D Channel DOT Fluence
0
20
40
60
80
100
PPL (mm)
2 Weeks, 1, 2, 3, & 4.5 Months
6, 7.5, 9, 10.5, & 12 Months
15 & 18 Months, 2 Years
4, 12 & 20-24 Years

B.

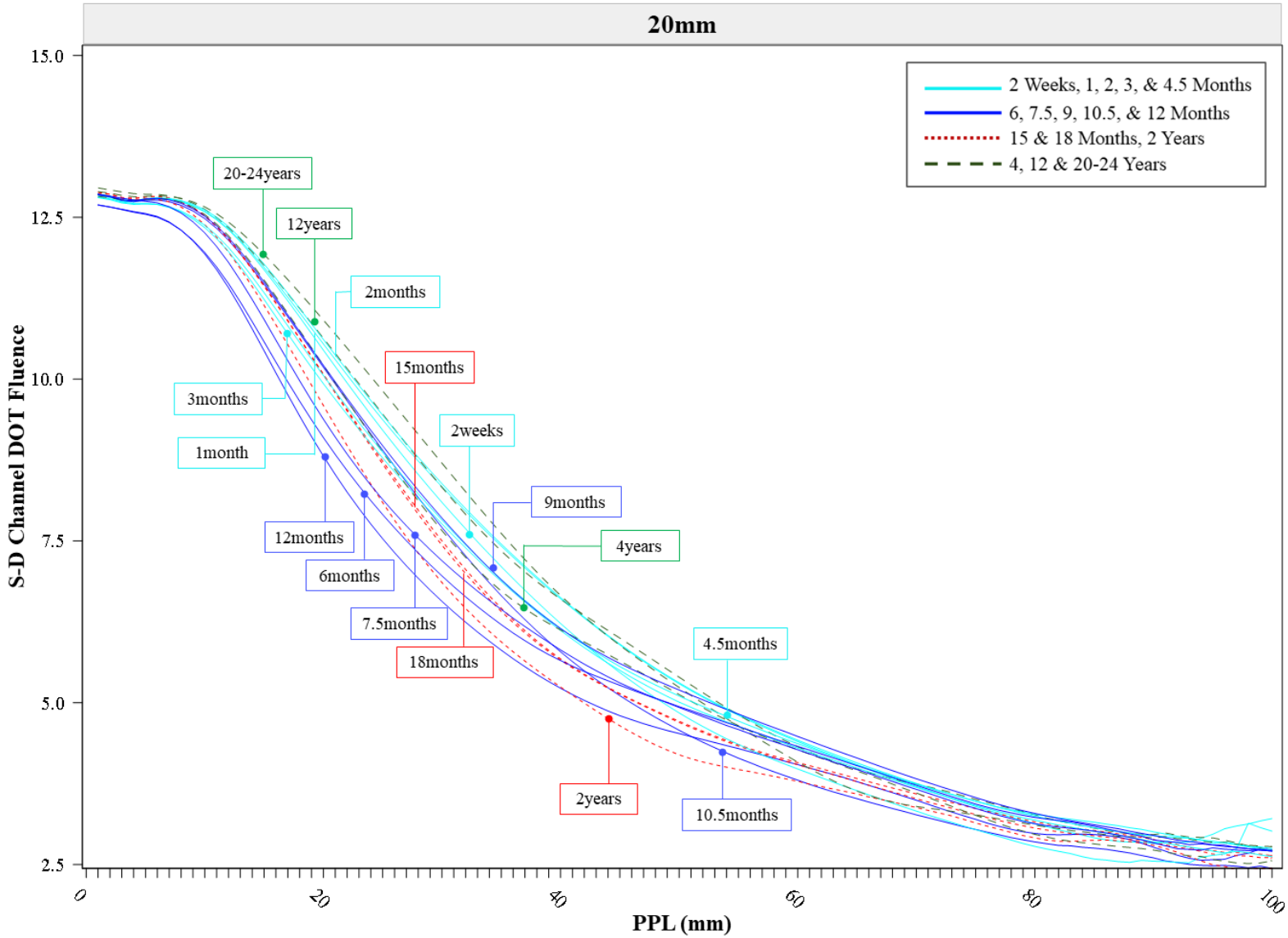
20mm
2 Weeks, 1, 2, 3, & 4.5 Months
6, 7.5, 9, 10.5, & 12 Months
15 & 18 Months, 2 Years
4, 12 & 20-24 Years
20-24years
12years
2months
15months
3months
2weeks
1month
9months
12months
4years
6months
7.5months
4.5months
18months
2years
10.5months
S-D Channel DOT Fluence
15.0
12.5
10.0
7.5
5.0
2.5
0
20
40
60
80
100
PPL (mm)

C.

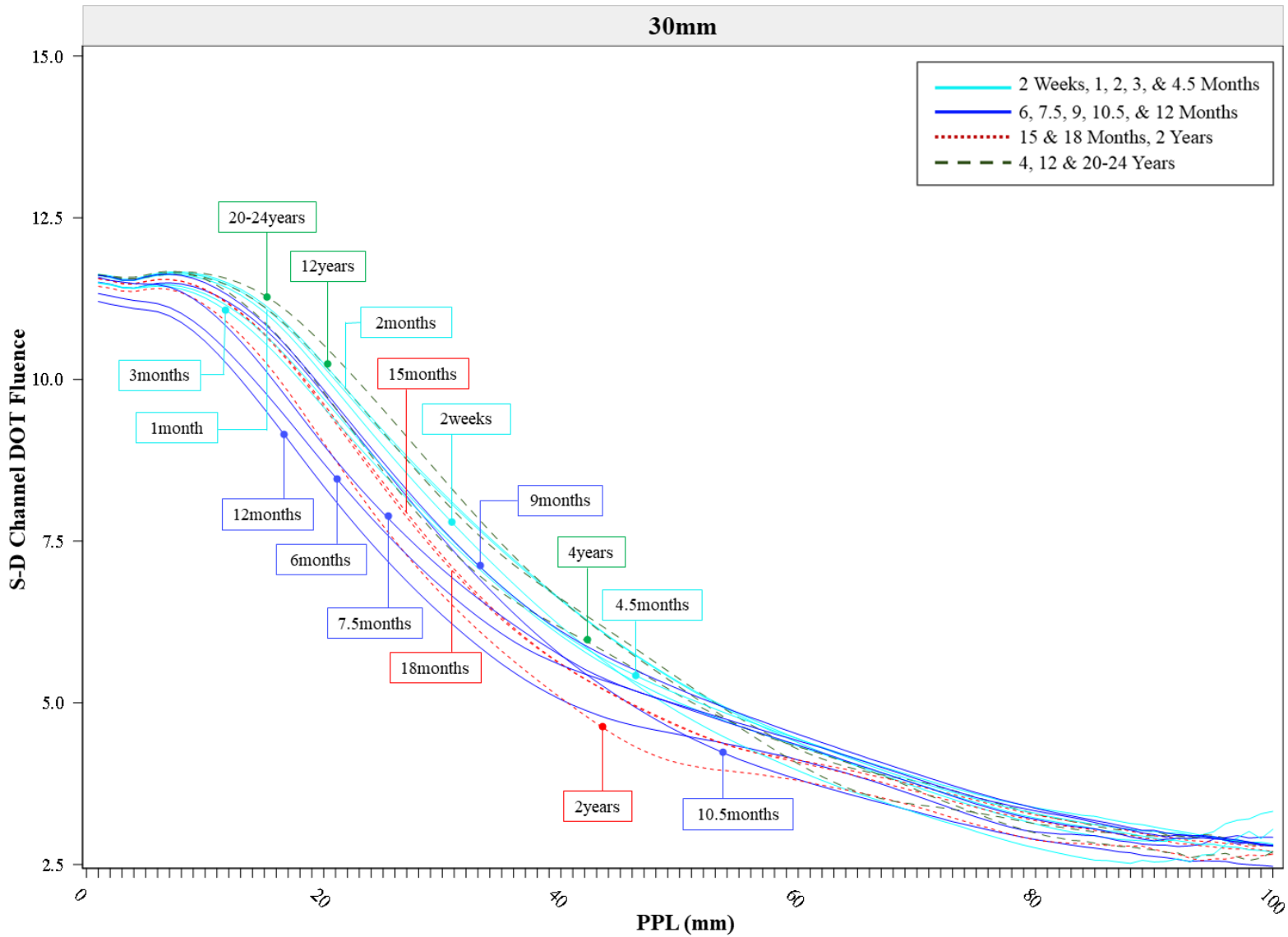
30mm
2 Weeks, 1, 2, 3, & 4.5 Months
6, 7.5, 9, 10.5, & 12 Months
15 & 18 Months, 2 Years
4, 12 & 20-24 Years
20-24years
12years
2months
3months
15months
1month
2weeks
9months
12months
6months
4years
4.5months
7.5months
18months
2years
10.5months
S-D Channel DOT Fluence
15.0
12.5
10.0
7.5
5.0
2.5
0
20
40
60
80
100
PPL (mm)

D.

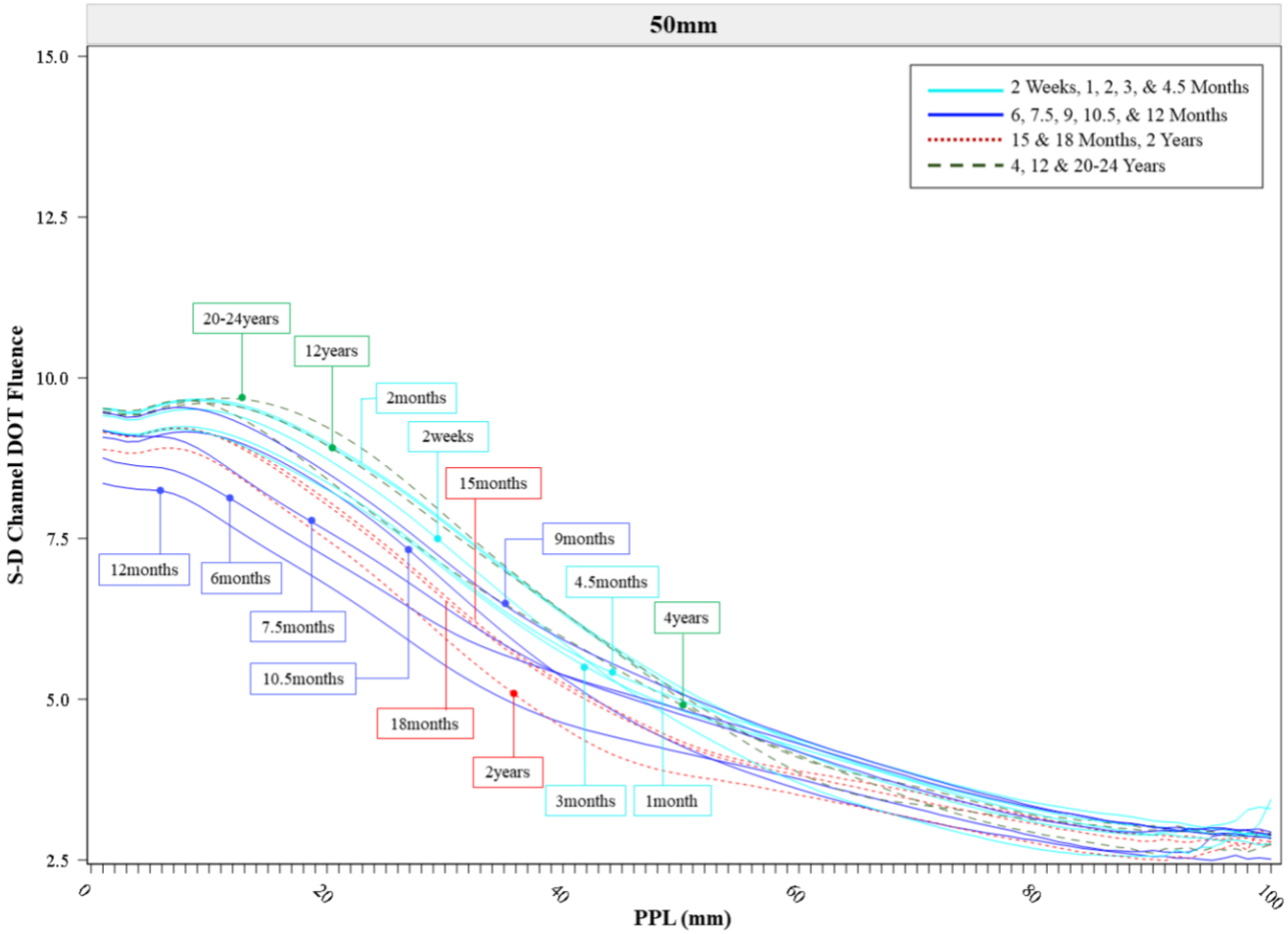

Fig 9. Source-Detector (S-D) Channel DOT fluence sensitivity profile by age groups. A. S-D Channel DOT fluence sensitivity function at each target source-detector separation distances. For visualization, we created four age categories: 2 weeks to 4.5 months, 6 months to 12 months, 15 months to 2 years, and 4 years to 20-24 years. Mean values by each age category are displayed. B. S-D Channel DOT fluence sensitivity function by individual age categories at 20 mm source-detector separation. C. S-D Channel DOT fluence sensitivity function by individual age categories at 30 mm separation. D. S-D Channel DOT fluence sensitivity function by individual age categories at 50 mm separation.

(Figure 9A solid line, aqua color) had a relatively high peak and rapid decline, the 6-month-to-12 month ages (Figure 9A solid line blue color) and the 15-month to 2-year-old ages (Figure 9A dashed line red color) had a smaller peak value and less rapid decline, i.e., flatter shape. These age differences were similar across all source-detector distances but became greater with increasing source-detector distance.

We also examined the between-channel variance of the S-D Channel DOT fluence as a function of penetration depths. Figure 8 showed the average between-channel variance of the sensitivity profiles across separation distances, which apparently differed across ages and showed a larger change with source-detector separation for infants than adults. We further examined the variance by computing the average standard error of the mean S-D Channel DOT fluence value. Figure 10A displays the average of the standard error as a function of PPL for each separation distance. The average variance as a function of penetration depth increased at separation distances greater than 35 mm for the younger infants (2 weeks to 12 months). The average variance became larger with increased penetration depth for the infants between 15 months to 2 years of age at separation distances greater than 20 mm. The average variance across penetration depth significantly increased at 55 mm and 60 mm separations for the 15-month-to-2-year group. The average variance across penetration depth remained relatively stable for the child and adult group. Figure 10B shows the standard error of the mean S-D Channel DOT fluence value as a function of penetration depth separately by the testing age groups at 20 mm separation. The variance across penetration depth was the greatest for infants aged between 3 months to 2 years relative to the children and adults. The youngest infants (2 weeks, 1 month, 2 months) showed relatively small variability across separation depts. We present similar figures for 30 mm and 50 mm separations in Supplemental Information Figures 10A and 10B. These

A.

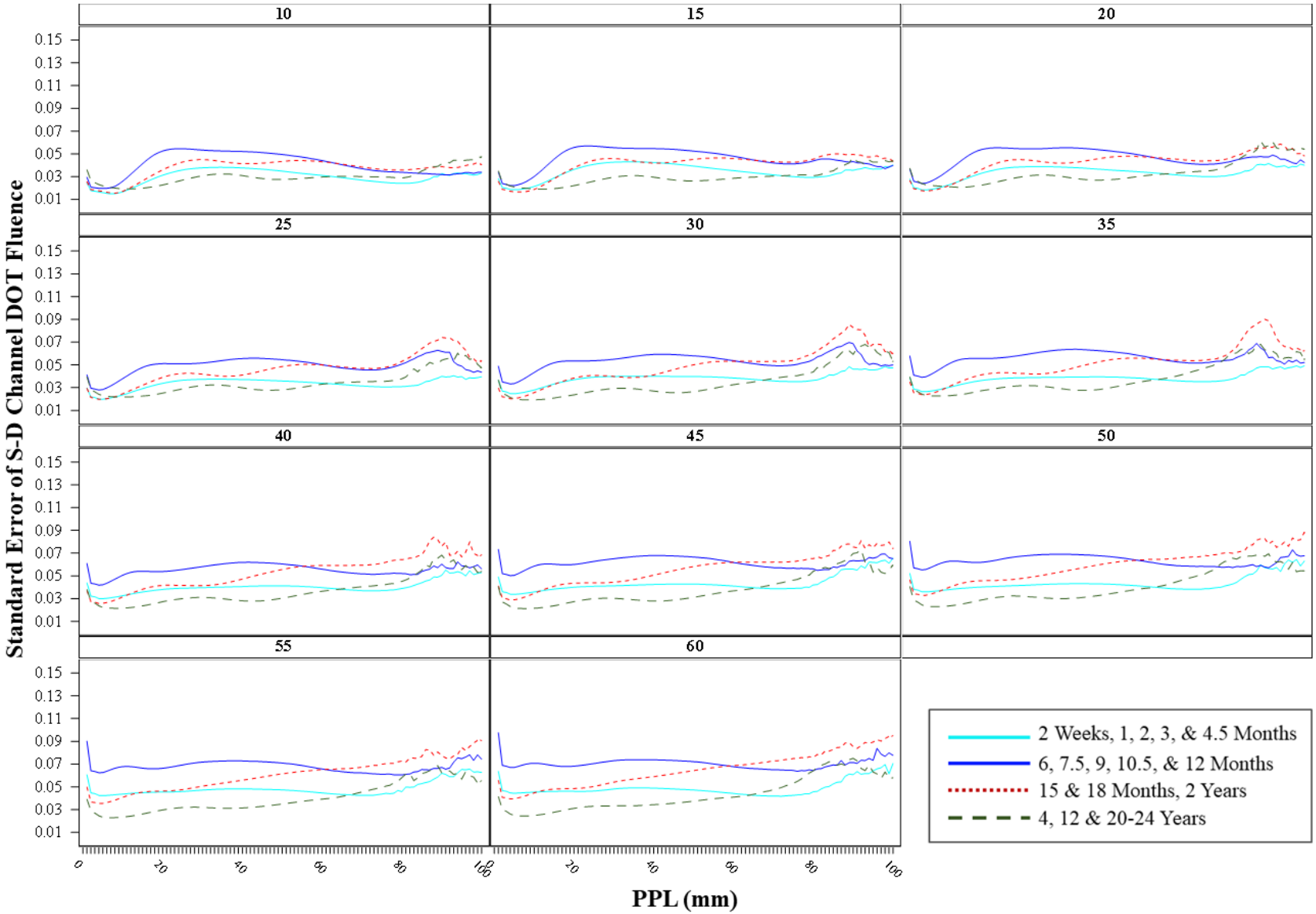
10
15
20
25
30
35
40
45
50
55
60
Standard Error of S-D Channel DOT Fluence
0.15
0.13
0.11
0.09
0.07
0.05
0.03
0.01
0
20
40
60
80
100
PPL (mm)
2 Weeks, 1, 2, 3, & 4.5 Months
6, 7.5, 9, 10.5, & 12 Months
15 & 18 Months, 2 Years
4, 12 & 20-24 Years

B.

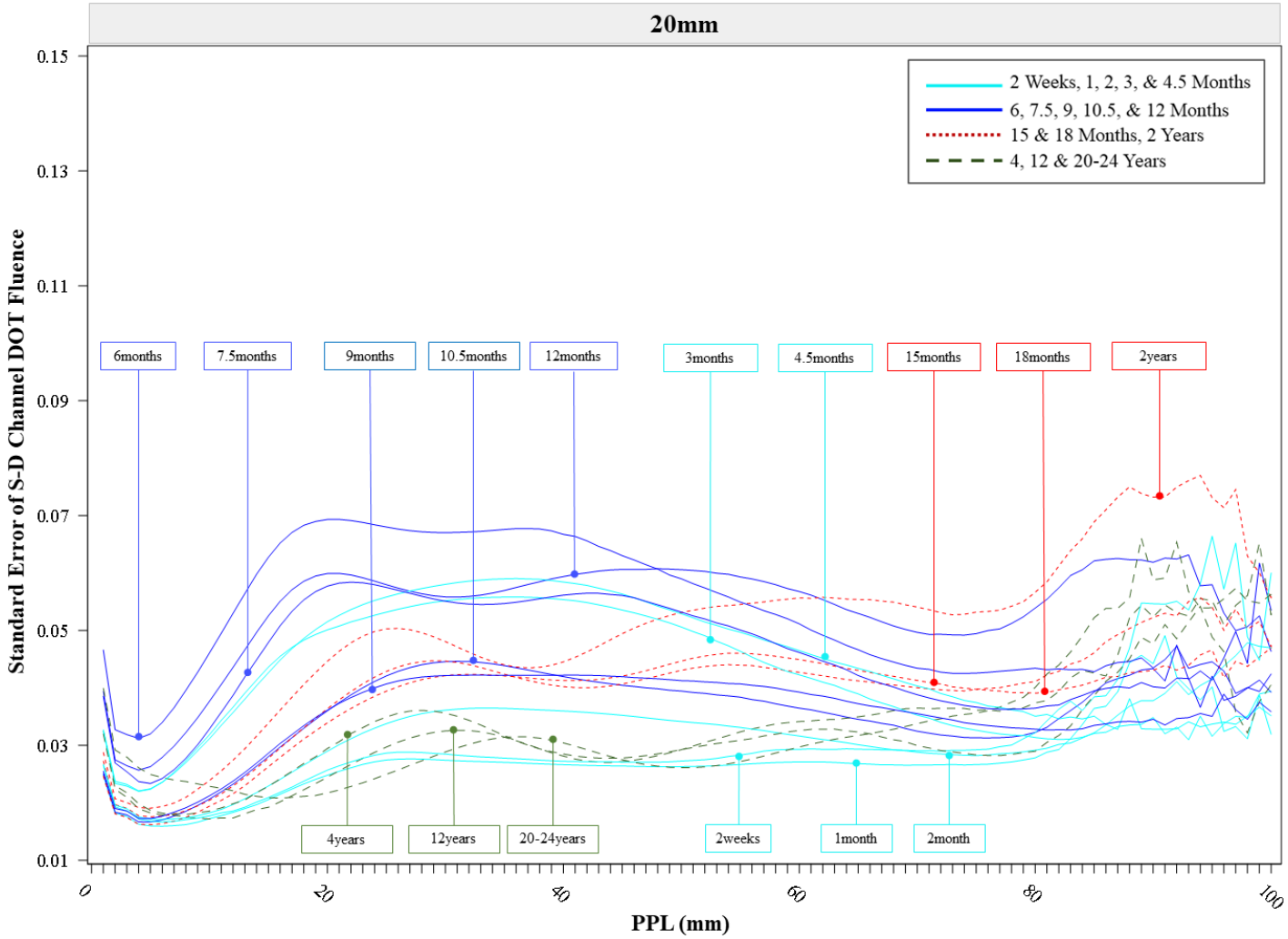

Fig 10. Variability of Source-Detector (S-D) Channel DOT fluence sensitivity profile. This is the standard error of the S-D Channel DOT fluence value as a function of the partial path length (PPL). A. Standard error of the S-D Channel DOT fluence sensitivity function averaged by the age categories. B. Standard error of the S-D Channel DOT fluence sensitivity function by individual age groups at 20 mm source-detector separation.

figures show that the variance as a function of penetration depth was greater at larger separations for all age groups. The age-related differences in variance were enhanced at 50 mm separations. The increase in variance at larger separation was more discernible for infants between 3 months to 2 years. The patterns of age-group differences in variance of the sensitivity profile across separation distances were consistent with the individual-subject plots displayed in Figure 8 and Supplemental Information Figure 9.

The last analysis examined the half-width half-maximum (HWHM) location for each S-D Channel DOT fluence distribution. Figure 11 shows the HWHM location as a function of the source-detector distance separately for the testing ages, separately for all ages (Figure 11A) and for four separate age groupings (Figure 11B). The HWHM increased as a function of the source-detector distance. This increase quantifies the apparent change in steepness in the S-D DOT Channel fluence sensitivity functions over source-detector distances (Figure 9A). The change in HWHM across source-detector distance implies that there was a gain in sensitivity to deeper cortex over the source-detector distance, though the fluence strength systematically decreased with increasing source-detector distance (e.g., Figure 9A). The patterns of the HWHM location over age parallel the age differences found in the sensitivity profile (e.g., Figure 9A). The mean HWHM locations across all separation distances were greater in the youngest infants (2-week through 4.5 month old age groups, Figure 11A and 11B solid line, aqua color), at smaller levels in the 6-month-to-12 month ages (Figure 11A and 11B solid line blue color) and the 15-month to 2-year-old ages (Figure 11A and 11B dashed line red color). These differences were consistent with the age differences found in the sensitivity profile (e.g., Figure 9A). The larger HWHM location values for the youngest age group implies the DOT sensitivity to deeper cortical areas for the youngest ages.

A.

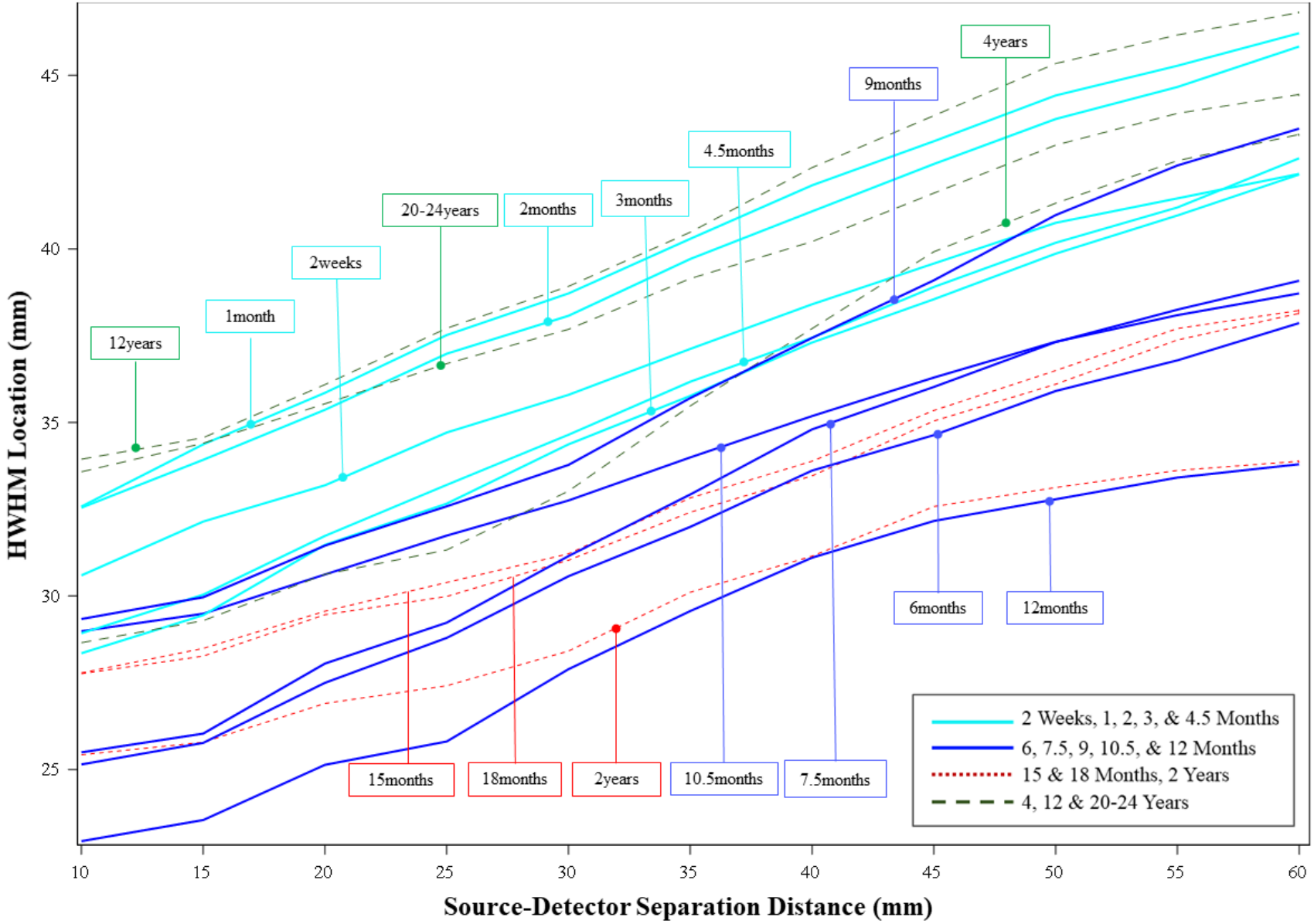
HWHM Location (mm)
Source-Detector Separation Distance (mm)
45
40
35
30
25
10
15
20
25
30
35
40
45
50
55
60
12years
1month
2weeks
20-24years
2months
3months
4.5months
9months
4years
15months
18months
2years
10.5months
7.5months
6months
12months
2 Weeks, 1, 2, 3, & 4.5 Months
6, 7.5, 9, 10.5, & 12 Months
15 & 18 Months, 2 Years
4, 12 & 20-24 Years

B.

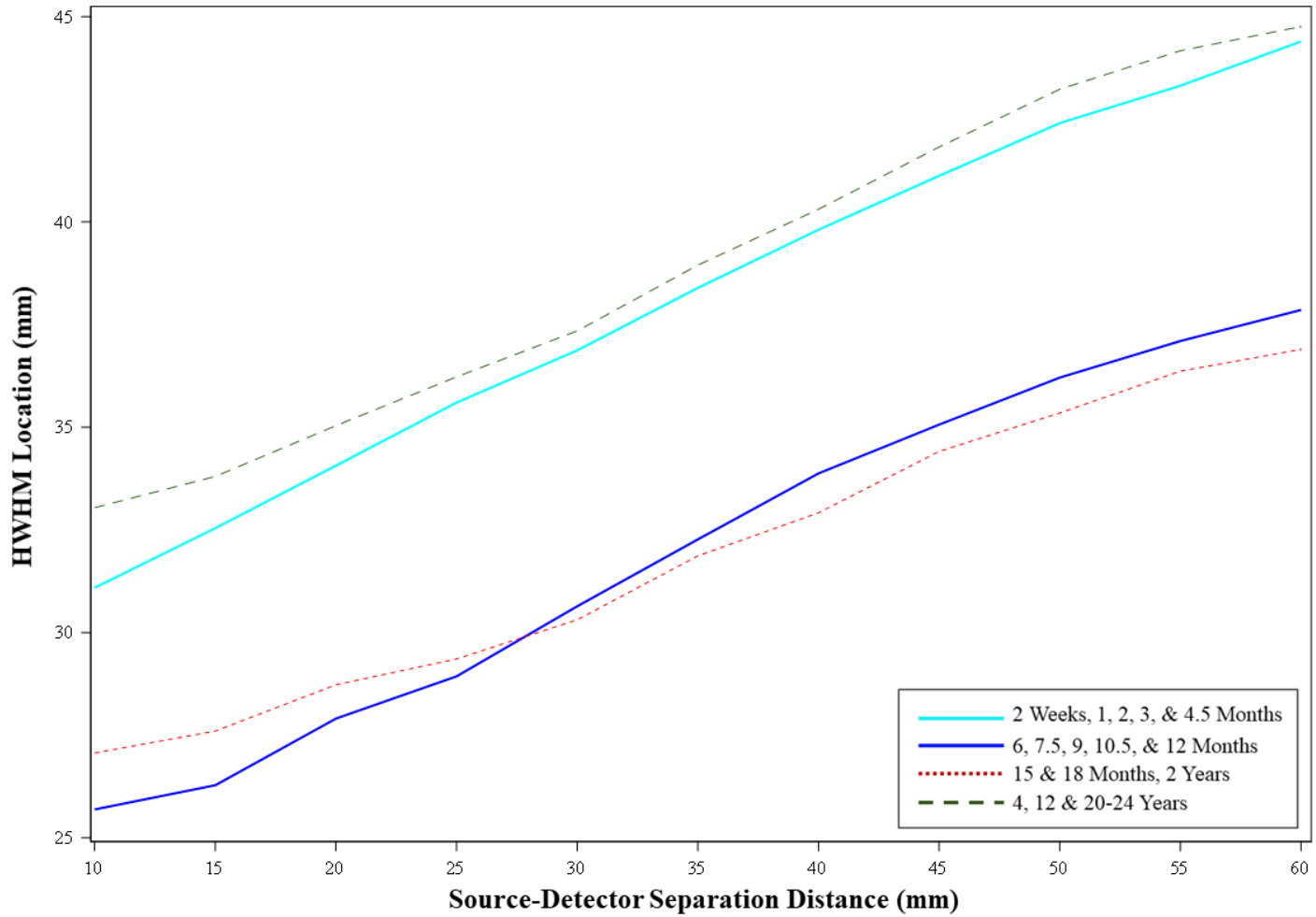

Fig 11. Half width half maximum (HWHM) locations of S-D Channel DOT fluence as a function of source-detector separation distances. The HWHM location was defined as the point in the fluence distribution at which the fluence first dropped below half of the maximum value. A. HWHM locations by source-detector separation distances for individual age groups. B. Mean HWHM locations by source-detector separation distances for the four age categories: 2 weeks to 4.5 months, 6 months to 12 months, 15 months to 2 years, and 4 years to 24 year.

Discussion

The present study examined age differences in scalp-to-cortex distances, scalp-location-to-ROI correspondence, and DOT sensitivity profiles. We extended existing co-registration and photon migration simulation methods to realistic head models from infants ranging from 2 weeks to 24 months, children (4, 12 years) and adults. The scalp-to-cortex distances increased from infancy to childhood and to adulthood. There were considerable variations in the distance measures among the infant age groups. The probabilistic mappings between scalp locations and cortical lobes were relatively stable across development. However, the mappings between scalp locations and cortical ROIs in sub-lobar atlas parcellations showed greater age-related variations. The DOT sensitivity profiles had a common shape across source-detector separation and ages. There were expected differences in the depth sensitivity for source-detector separations, with larger separations being more sensitivity to greater cortical depths but showing decreasing signal strength with source-detector distances. A noticeable age-group difference was that the fluence distribution penetrated greater depth with the same level of signal loss in the younger infant (2 weeks to 4.5months) than the rest of the infant age groups. We found that individual participant MRIs and average MRI templates from the Neurodevelopmental MRI Database (Richards, in prep; Richards, Sanchez, et al., 2015; Sanchez et al., 2012a, 2012b) were similar in their scalp-to-cortex distances.

Scalp-to-Cortex Distance

Three methods were used to measure scalp-to-cortex distances. The Scalp Projection method has been commonly adopted in developmental and adult studies to measure the anatomical distance between scalp electrode locations and the cortical surface (Beauchamp et al., 2011; Emberson et al., 2017; Kabdebon et al., 2014; Okamoto et al., 2004; Whiteman et al.,

2017). We also estimated the distance between the scalp location and the maximum source-detector fluence for the "Direct DOT" (2D Green's function) fluence distribution. The distances for these two measures were very similar. This is likely due to the monotonic and somewhat non-linear photon decay distribution across the head (Figure 9A) which is maximal near the surface of the cortex. The S-D Channel DOT fluence distances were greater than distances estimated from the other methods across scalp locations for all age groups. The S-D Channel DOT fluence represents the flow of photons from the source to the detector and was deeper than the cortical surface (Scalp Projection) or the photon flow from the optode source injection point (Direct DOT). All three estimation methods indicated that scalp-to-cortex distances averaged across the scalp locations increased from infancy to childhood and from childhood to adulthood. This finding is consistent with Beauchamp et al. (2011) who measured whole-brain distances from the scalp in newborns through 12-year-olds and other studies that measured scalp-to-cortex distances by electrode positions (3.4- to 16.3-week-olds; Kabdebon et al., 2014; 22- to 51-year-olds; Okamoto et al., 2004; 5- to 11-year-olds; Whiteman et al., 2017). The increase in scalp-to-cortex distances from infancy to adulthood may be attributed to several types of changes in the structure of the head. These include skull thickness (Emberson, Crosswhite, Goodwin, Berger, & Aslin, 2016; Hansman, 1966), increases in CSF volume (Makropoulos et al., 2016), global brain volume and gray matter / white matter growth (Gilmore et al., 2011; Makropoulos et al., 2016; Richards & Conte, 2020; Richards & Xie, 2015), and cortical folding during the first 2 years (Li et al., 2014). Brain structural growth is more gradual during childhood and adolescence and reaches plateau during adulthood (Brain Development Cooperative Group, 2011; Raznahan et al., 2011; Richards & Conte, 2020; Richards & Xie, 2015).

There were between-electrode variations in scalp-to-cortex distance, and these variations were heterogeneous among infant groups. The Scalp Projection and S-D Channel DOT distances for all age groups were greatest at the frontal and central electrodes on the bottom row around the face area, followed by electrode locations at the midline along the intra-hemispherical fissure, and the smallest on the electrode locations internal to these edges. Such inter-electrode variations were also found in previous studies (Kabdebon et al., 2014; Okamoto et al., 2004; Whiteman et al., 2017). Furthermore, we extended prior findings with young infants (Kabdebon et al., 2014) and revealed that there was a prominent decrease in distances from anterior to posterior locations in some infant groups (Scalp Projection distances in 3- to 10.5-month-olds and S-D Channel DOT distances in 2-week- to 10.5-month, 15-month, and 18-month-olds). This anterior-to posterior decrease in distance was less discernible in other age groups including adults (Okamoto et al., 2004). The anterior-posterior gradient coincides with the posterior-to-anterior sequence of cortical maturation (Brain Development Cooperative Group, 2011; Gilmore et al., 2007). The occipital and parietal lobes show faster growth in volume during infancy than the frontal regions (Gilmore et al., 2007). This implies that the posterior regions have expanded closer to the scalp surface earlier than anterior regions. In contrast, there is more significant age-related decline in occipital and parietal lobes than the frontal lobe from childhood to young adulthood (Brain Development Cooperative Group, 2011). The region-specific heterogeneous patterns of brain development that are observable from infancy (e.g. Gilmore et al., 2007; Gilmore et al., 2011; Li, Lin, Gilmore, & Shen, 2015; Makropoulos et al., 2016; Remer et al., 2017) may contribute to the lack of systematic age-related increase in scalp-to-cortex distances among infant groups. Together, the Scalp Projection and DOT fluence measures of scalp-to-cortex distances are sensitive to the complex age- and region-dependent cortical growth.

Gauging scalp-to-cortex distance is a foundational step for optimizing DOT sensitivity to the target cortical regions. Greater scalp-to-cortex distance is associated with reduced DOT sensitivity to the brain (Strangman et al., 2014; Whiteman et al., 2017) when the source-detector separation distance is fixed. This implies that there would be age-related changes in the depth sensitivity for NIRS recordings with source-detector channels placed at the same distances for young and older participants. It is therefore a common practice to use shorter separations for infants compare to adults (Gervain et al., 2011; Pinti et al., 2020). Increasing the separation distance allows the fluence distribution to extend deeper into the head tissues and thus sample cortical regions at greater depth (Mansouri et al., 2010; Strangman et al., 2013; Strangman et al., 2014; Wang et al., 2019). However, the increased depth sensitivity is at the expense of decreased signal strength (Wang et al., 2019). Our results with the depth sensitivity profiles could be used to find similar depth sensitivity with differing source-detector separations for participants at different ages.

Age-appropriate MRI templates may be used to describe cranio-cerebral correspondence when subjects' own MRIs are unavailable. The present study showed that the age-appropriate templates has comparable S-D Channel DOT distances as the individual head models. Furthermore, the S-D Channel DOT distance estimations were robust across different Monte Carlo simulation methods (MCX, MMC, and tMCimg) for 3-month and 6-month infants' individual MRIs and age-appropriate average templates (Supplemental Information Figure 6, 7, and 8). The developmental differences in scalp-to-cortex distances suggest that adult head models should not be used to make anatomical inferences for infant or child standalone NIRS/fNIRS data. We recommend using age-appropriate average templates or the individual

MRIs when the subject's own MRIs are not collected (e.g. Emberson, Cannon, et al., 2016; Emberson et al., 2017; Emberson et al., 2015).

Scalp-location-to-ROI Mapping

This is the first study that provided scalp-location-to-ROI look-up tables computed using multiple methods for a wide range of age groups. We used the Scalp Projection and the S-D Channel DOT fluence to map 10-10 scalp electrode/channel locations with underlying ROIs from a macrostructural atlas (lobar) and two sublobar atlases (Hammers and LPBA40). The Spatial Projection method mapped underlying ROIs based only on the spatial anatomical relations. The S-D Channel DOT method mapped underlying ROIs based on the DOT fluence sensitivity profile. The S-D Channel-DOT look-up table supported the prior finding that there is consistent correspondence between the majority of scalp locations and macrostructural ROIs for infants (Kabdebon et al., 2014; Lloyd-Fox et al., 2014) and adults (Koessler et al., 2009; Okamoto et al., 2004). For smaller sub-lobar atlas ROIs, some channel locations show consistent correspondence between scalp location and underlying cortical ROI. For example, F5 and F6 were corresponded to bilateral inferior and middle frontal gyrus in all age groups. However, many channel locations show inconstant mappings across age groups. These include posterior midline positions and frontal channels on the bottom row where the scalp-to-cortex distance was larger. For example, channel TP7 was sensitive to both the inferior and middle temporal gyrus in the LPBA40 atlas for age 2 weeks through 12 years whereas it was mapped to only the middle temporal gyrus for 20-24-year-olds. Therefore, it is important to use age-appropriate head models to fully account for the age-dependent head and cortical structural changes when examining cranio-cerebral correspondence.

The age-appropriate S-D Channel DOT look-up procedures can be adopted to localize the ROI(s) that generate the fNIRS activities and design the optode arrangement prior to data collection. Our findings highlight a recognized issue in fNIRS data interpretation: the channel(s) that show significant activations from the group analysis may not correspond to the same ROI for all participants (Powell, Deen, & Saxe, 2018). This problem is especially concerning for infant and child studies that encompass a wide age range. Our S-D Channel DOT look-up procedures provide an effective solution. The optode locations recorded from an experiment can be co-registered with individual head models from infants closely matched in age and head measurements, if subjects' own MRIs are not available. S-D Channel DOT sensitivity is then estimated to infer the subject-specific ROI(s) that have generated the fNIRs signals. The methodological details were also presented elsewhere (Bulgarelli et al., 2019; Bulgarelli et al., 2020; Perdue et al., 2019).

Our method and tables may also be used to design optode placement on NIRS holders that maximize channel sensitivity to hemodynamic changes of underlying ROIs. The tables we provide for the 10-10 or 10-5 recording system can be used as lookup tables for either manual construction of optode locations or used with automatic methods. We additionally provided age-apropriate S-D Channel DOT look-up table that quantify the sensitivity of channel pairings from the fOLD toolbox (Zimeo Morais et al., 2018) to lobar and sub-lobar ROIs (Supplemental Information Table 4). The table provides the specificity (%) of the channel to the ROI out of the total S-D Channel DOT sensitivity to all ROIs in the atlas. Researchers can thus design their holders to include channels that are sensitive to the user-specified ROIs with a specificity threshold (Zimeo Morais et al., 2018). Supplemental Information Figure 3D presents an example

of optode placement that includes channels sensitive to the left inferior frontal gyrus with specificity greater than 1% for 6-month infants.

DOT Depth Sensitivity Profiles

The present study showed that the depth sensitivity profiles change systematically as a function of source-detector separation distance for all age groups. The study enhanced the DOT sensitivity estimation accuracy by using realistic FEM head models with refined segmentation of tissue types. The depth sensitivity profiles depict S-D Channel DOT fluence as a function of PPL sampled in the fluence distribution. The peak value of the S-D Channel DOT fluence was larger at shorter separation distances but with rapid decay as PPL increased. Alternatively, at larger separation distances there was a smaller peak value but with less rapid decline with increased PPL. The between-channel variance in the sensitivity profiles considerably increased with separation distances in infants. The increase was greater in older infants between 3 months to 2 years. The variance remained relatively stable for younger infants (2 weeks to 2 months), children, and adults.

The shape of the sensitivity profile was characterized by measuring the point in the fluence distribution where the fluence value first dissipated below half of the maximum value (i.e. “HWHM location”). The HWHM location increased with source-detector separation distance for all age groups. This indicates that there is a gain in sensitivity to deeper cortical structures with increased separations at the expense of decreased signal strength. We replicated the robust characteristics of the DOT sensitivity profiles found in existing studies that modeled photon migrations in head models from infants (Fukui et al., 2003) and adults (Mansouri et al., 2010; Strangman et al., 2013; Strangman et al., 2014; Wang et al., 2019). The trade-off between

the gain in sensitivity to deeper cortical regions and loss in signal strength and spatial resolution needs to be considered in the design of source-detector separation distances.

The depth sensitivity profiles showed relatively consistent age-related differences across source-detector separation distances. Young infant groups (2 weeks to 4.5 months) displayed a sensitivity profile that was significantly different from the older infant groups (6 months to 2 years). The sensitivity profiles for the young infant groups at all separation distances were characterized by higher peaks and steeper decreases of S-D Channel DOT fluence values with increased PPL. Their sensitivity profiles displayed relatively stable variance across separation distances. The sensitivity profiles for the older infant groups were characterized by smaller peaks and more gradual declines with increased PPL. Their sensitivity profiles showed greater variance at larger separations. The slopes of increase in HWHM location across source-detector distance were similar across age groups. This suggests that the gain in depth sensitivity by increasing separation distances is comparable across age groups. fNIRS studies conventionally use 20mm to 30mm separations for infants (Gervain et al., 2011; Lloyd-Fox, Blasi, & Elwell, 2010) and 30mm to 35mm for children (e.g. Ding, Fu, & Lee, 2014; Perlman, Luna, Hein, & Huppert, 2014) and adults (Pinti et al., 2020). We showed that young infants displayed comparable DOT sensitivity profiles at 20mm-to-30mm separation but had closer scalp-to-cortex distances compared to adults. Hence, young infants may have greater DOT sensitivity to the cortex than adults (cf. Fukui et al., 2003). The main effect of age groups was more discernible at larger separations. Increasing separation distances to 35mm or greater may cause more concern in terms of reduction of signal strength and increased variance with relatively less gain in improving sensitivity to the cortex for older infants compared to adults.

The age-related differences in sensitivity profiles reinforce the importance of using age-appropriate head models for estimating forward models of DOT sensitivity. The sensitivity profile estimated from MC photon migration simulations can be recorded in a forward matrix. This is then used for solving the inverse problem in DOT image reconstruction that localizes the ROIs that showed hemoglobin concentration changes (Cooper et al., 2012; Culver et al., 2003). Contemporary toolboxes for DOT image source reconstruction (AtlasViewer: Aasted et al., 2015; TOAST++: Schweiger & Arridge, 2014) use adult head models as the default option. The present study provides data that show the importance of using age-appropriate templates as an anatomical prior to improve accuracy in channel location co-registration and forward model estimation. Wijeakumar, Kumar, Delgado Reyes, Tiwari, and Spencer (2019) and Delgado Reyes, Wijeakumar, Magnotta, Forbes, and Spencer (2020) show examples of this. They selected head models with atlas parcellations from the Neurodevelopmental MRI database (Richards, in prep; Richards, Sanchez, et al., 2015; Sanchez et al., 2012a, 2012b) that were closely matched in age of the participants (4-month to 2-year-olds: Delgado Reyes et al., 2020; 4- to 48-month-olds: Wijeakumar et al., 2019). The head models were used for estimating the forward model and image reconstruction using the AtlasViewer (Aasted et al., 2015). The resultant voxel-wise hemodynamic concentration estimates were then entered in group-level analyses.

Limitation

The current study did not compute DOT sensitivity by tissue types separately. Existing evidence indicated that the change of relative sensitivity as a function of source-detector separation distance displayed different shapes for GM, WM, CSF, and extracerebral tissues (scalp and skull) in infants and adults (Fukui et al., 2003; Mansouri et al., 2010; Strangman et al., 2013; Strangman et al., 2014). Our data could be used to evaluate the fluence strength to the

cortex based on the S-D Channel DOT scalp-to-cortex distance and the depth sensitivity profiles. We also could directly compare the relative sensitive to the brain versus extracerebral tissues at different separation distances for infants and adults (Brigadoi & Cooper, 2015; Strangman et al., 2013). Future analyses that compare sensitivity profiles by tissue types could more precisely inform age-related differences in the optimal separation distances for sampling GM signal changes.

Conclusions

The current study examined scalp-to-cortex distances, scalp-to-cortical ROI correspondence, and DOT sensitivity profiles in infants, children, and adults. There were differences in the scalp-to-cortex distance in infants, which become magnified in children and adults. We found systematic differences in scalp-location-to-anatomical ROI correspondence for different ages, both for spatial projection and for DOT fluence sensitivity. There were age-related differences in the DOT fluence depth sensitivity profile across a large range of source-detector channel separations. Our findings of age-related differences in DOT depth sensitivity profiles are useful in the analysis of age-appropriate source-detector distances that match sensitivity, signal strength, and depth for different ages. Our findings imply that accurate anatomical interpretations of NIRS/fNIRS data are dependent on developmentally-sensitive estimations of DOT sensitivity that account for the head and cortical development. The present study demonstrated that age-appropriate realistic head models can be used with spatial scalp projection and photon migration simulations to provide anatomical guidance for standalone DOT data.

Acknowledgement

This research was supported by grants from the National Institute of Child Health and Human Development (NICHD-R01-HD18942, NICHD-R37-HD18942, NIHCD-R03-HD091464) to J.E. Richards.

References

Aasted, C., Yücel, M., Cooper, R., Dubb, J., Tsuzuki, D., Becerra, L., . . . Boas, D. (2015). Anatomical guidance for functional near-infrared spectroscopy: AtlasViewer tutorial. *Neurophotonics, 2*(2), 020801.

Avants, B. B., Tustison, N. J., Song, G., Cook, P. A., Klein, A., & Gee, J. C. (2011). A reproducible evaluation of ANTs similarity metric performance in brain image registration. *Neuroimage, 54*(3), 2033-2044. doi:https://doi.org/10.1016/j.neuroimage.2010.09.025

Beauchamp, M. S., Beurlot, M. R., Fava, E., Nath, A. R., Parikh, N. A., Saad, Z. S., . . . Oghalai, J. S. (2011). The Developmental Trajectory of Brain-Scalp Distance from Birth through Childhood: Implications for Functional Neuroimaging. *PLOS ONE, 6*(9), e24981. doi:10.1371/journal.pone.0024981

Boas, D. A., Culver, J. P., Stott, J. J., & Dunn, A. K. (2002). Three dimensional Monte Carlo code for photon migration through complex heterogeneous media including the adult human head. *Opt Express, 10*, 159-170.

Brain Development Cooperative Group. (2011). Total and Regional Brain Volumes in a Population-Based Normative Sample from 4 to 18 Years: The NIH MRI Study of Normal Brain Development. *Cerebral Cortex, 22*(1), 1-12. doi:10.1093/cercor/bhr018

Brigadoi, S., Aljabar, P., Kuklisova-Murgasova, M., Arridge, S. R., & Cooper, R. J. (2014). A 4D neonatal head model for diffuse optical imaging of pre-term to term infants. *Neuroimage, 100*, 385-394. doi:10.1016/j.neuroimage.2014.06.028

Brigadoi, S., & Cooper, R. J. (2015). How short is short? Optimum source-detector distance for short-separation channels in functional near-infrared spectroscopy. *Neurophotonics, 2*(2), 025005. doi:10.1117/1.NPh.2.2.025005

Brigadoi, S., Salvagnin, D., Fischetti, M., & Cooper, R. (2018). Array Designer: automated optimized array design for functional near-infrared spectroscopy. *Neurophotonics, 5*(3), 035010.

Bulgarelli, C., Blasi, A., de Klerk, C. C. J. M., Richards, J. E., Hamilton, A., & Southgate, V. (2019). Fronto-temporoparietal connectivity and self-awareness in 18-month-olds: A resting state fNIRS study. *Developmental Cognitive Neuroscience, 38*, 100676. doi:https://doi.org/10.1016/j.dcn.2019.100676

Bulgarelli, C., de Klerk, C. C. J. M., Richards, J. E., Southgate, V., Hamilton, A., & Blasi, A. (2020). The developmental trajectory of fronto-temporoparietal connectivity as a proxy of the default mode network: a longitudinal fNIRS investigation. *Human Brain Mapping, 41*(10), 2717-2740. doi:10.1002/hbm.24974

Cooper, R. J., Caffini, M., Dubb, J., Fang, Q., Custo, A., Tsuzuki, D., . . . Boas, D. A. (2012). Validating atlas-guided DOT: a comparison of diffuse optical tomography informed by atlas and subject-specific anatomies. *Neuroimage, 62*(3), 1999-2006. doi:10.1016/j.neuroimage.2012.05.031

Culver, J. P., Siegel, A. M., Stott, J. J., & Boas, D. A. (2003). Volumetric diffuse optical tomography of brain activity. *Optics Letters, 28*(21), 2061-2063. doi:10.1364/ol.28.002061

Custo, A., Boas, D. A., Tsuzuki, D., Dan, I., Mesquita, R., Fischl, B., . . . Wells, W., 3rd. (2010). Anatomical atlas-guided diffuse optical tomography of brain activation. *Neuroimage, 49*(1), 561-567. doi:10.1016/j.neuroimage.2009.07.033

Delgado Reyes, L., Wijeakumar, S., Magnotta, V. A., Forbes, S. H., & Spencer, J. P. (2020). The functional brain networks that underlie visual working memory in the first two years of life. *Neuroimage, 219*, 116971. doi:https://doi.org/10.1016/j.neuroimage.2020.116971

Di Martino, A., Yan, C. G., Li, Q., Denio, E., Castellanos, F. X., Alaerts, K., . . . Milham, M. P. (2014). The autism brain imaging data exchange: towards a large-scale evaluation of the intrinsic brain architecture in autism. *Mol Psychiatry, 19*(6), 659-667. doi:10.1038/mp.2013.78

Ding, X. P., Fu, G., & Lee, K. (2014). Neural correlates of own- and other-race face recognition in children: A functional near-infrared spectroscopy study. *Neuroimage, 85*, 335-344. doi:https://doi.org/10.1016/j.neuroimage.2013.07.051

Douaud, G., Smith, S., Jenkinson, M., Behrens, T., Johansen-Berg, H., Vickers, J., . . . James, A. (2007). Anatomically related grey and white matter abnormalities in adolescent-onset schizophrenia. *Brain, 130*(9), 2375-2386. doi:10.1093/brain/awm184

Emberson, L. L., Cannon, G., Palmeri, H., Richards, J. E., & Aslin, R. N. (2016). Using fNIRS to Examine Occipital and Temporal Responses to Stimulus Repetition in Young Infants: Evidence of Selective Frontal Cortex Involvement. *Developmental Cognitive Neuroscience*.

Emberson, L. L., Crosswhite, S. L., Goodwin, J. R., Berger, A. J., & Aslin, R. N. (2016). Isolating the effects of surface vasculature in infant neuroimaging using short-distance optical channels: a combination of local and global effects. *Neurophotonics, 3*(3), 031406-031406. doi:10.1117/1.NPh.3.3.031406

Emberson, L. L., Crosswhite, S. L., Richards, J. E., & Aslin, R. N. (2017). The Lateral Occipital Cortex Is Selective for Object Shape, Not Texture/Color, at Six Months. *Journal of Neuroscience, 37*(13), 3698-3703. doi:10.1523/jneurosci.3300-16.2017

Emberson, L. L., Richards, J. E., & Aslin, R. N. (2015). Top-down modulation in the infant brain: Learning-induced expectations rapidly affect the sensory cortex at 6 months. *Proceedings of the National Academy of Sciences of the United States of America, 112*(31), 9585–9590. doi:10.1073/pnas.1510343112

Fang, Q. (2010). Mesh-based Monte Carlo method using fast ray-tracing in Plücker coordinates. *Biomedical Optics Express, 1*(1), 165-175. doi:10.1364/boe.1.000165

Fang, Q., & Boas, D. A. (2009a). Monte Carlo simulation of photon migration in 3D turbid media accelerated by graphics processing units. *Opt Express, 17*(22), 20178-20190. doi:10.1364/oe.17.020178

Fang, Q., & Boas, D. A. (2009b, 28 June-1 July 2009). *Tetrahedral mesh generation from volumetric binary and grayscale images.* Paper presented at the 2009 IEEE International Symposium on Biomedical Imaging: From Nano to Macro.

Fang, Q., & Yan, S. (2019). Graphics processing unit-accelerated mesh-based Monte Carlo photon transport simulations. *Journal of Biomedical Optics, 24*(11), 115002.

Fekete, T., Rubin, D., Carlson, J. M., & Mujica-Parodi, L. R. (2011). A stand-alone method for anatomical localization of NIRS measurements. *Neuroimage, 56*(4), 2080-2088. doi:https://doi.org/10.1016/j.neuroimage.2011.03.068

Fillmore, P. T., Phillips-Meek, M. C., & Richards, J. E. (2015). Age-specific MRI brain and head templates for healthy adults from 20 through 89 years of age. *Front Aging Neurosci, 7*, 44. doi:10.3389/fnagi.2015.00044

Fillmore, P. T., Richards, J. E., Phillips-Meek, M. C., Cryer, A., & Stevens, M. (2015). Stereotaxic Magnetic Resonance Imaging Brain Atlases for Infants from 3 to 12 Months. *Developmental Neuroscience, 37*(6), 515-532. doi:10.1159/000438749

Fukui, Y., Ajichi, Y., & Okada, E. (2003). Monte Carlo prediction of near-infrared light propagation in realistic adult and neonatal head models. *Applied Optics, 42*(16), 6.

Gervain, J., Mehler, J., Werker, J. F., Nelson, C. A., Csibra, G., Lloyd-Fox, S., . . . Aslin, R. N. (2011). Near-infrared spectroscopy: A report from the McDonnell infant methodology consortium. *Developmental Cognitive Neuroscience, 1*(1), 22-46. doi:https://doi.org/10.1016/j.dcn.2010.07.004

Gilmore, J. H., Lin, W., Prastawa, M. W., Looney, C. B., Vetsa, Y. S. K., Knickmeyer, R. C., . . . Gerig, G. (2007). Regional Gray Matter Growth, Sexual Dimorphism, and Cerebral Asymmetry in the Neonatal Brain. *The Journal of Neuroscience, 27*(6), 1255. doi:10.1523/JNEUROSCI.3339-06.2007

Gilmore, J. H., Schmitt, J. E., Knickmeyer, R. C., Smith, J. K., Lin, W., Styner, M., . . . Neale, M. C. (2010). Genetic and environmental contributions to neonatal brain structure: A twin study. *Human Brain Mapping, 31*(8), 1174-1182. doi:10.1002/hbm.20926

Gilmore, J. H., Shi, F., Woolson, S. L., Knickmeyer, R. C., Short, S. J., Lin, W., . . . Shen, D. (2011). Longitudinal Development of Cortical and Subcortical Gray Matter from Birth to 2 Years. *Cerebral Cortex, 22*(11), 2478-2485. doi:10.1093/cercor/bhr327

Gousias, I. S., Rueckert, D., Heckemann, R. A., Dyet, L. E., Boardman, J. P., Edwards, A. D., & Hammers, A. (2008). Automatic segmentation of brain MRIs of 2-year-olds into 83 regions of interest. *Neuroimage, 40*(2), 672-684. doi:10.1016/j.neuroimage.2007.11.034

Haeussinger, F. B., Heinzel, S., Hahn, T., Schecklmann, M., Ehlis, A.-C., & Fallgatter, A. J. (2011). Simulation of Near-Infrared Light Absorption Considering Individual Head and Prefrontal Cortex Anatomy: Implications for Optical Neuroimaging. *PLOS ONE, 6*(10), e26377. doi:10.1371/journal.pone.0026377

Hansman, C. F. (1966). Growth of Interorbital Distance and Skull Thickness as Observed in Roentgenographic Measurements. *Radiology, 86*(1), 87-96. doi:10.1148/86.1.87

Hazlett, H. C., Gu, H., Munsell, B. C., Kim, S. H., Styner, M., Wolff, J. J., . . . Statistical, A. (2017). Early brain development in infants at high risk for autism spectrum disorder. *Nature, 542*(7641), 348-351. doi:10.1038/nature21369

Heckemann, R. A., Hajnal, J. V., Aljabar, P., Rueckert, D., & Hammers, A. (2006). Automatic anatomical brain MRI segmentation combining label propagation and decision fusion. *Neuroimage, 33*(1), 115-126. doi:https://doi.org/10.1016/j.neuroimage.2006.05.061

Howell, B. R., Styner, M. A., Gao, W., Yap, P.-T., Wang, L., Baluyot, K., . . . Elison, J. T. (2019). The UNC/UMN Baby Connectome Project (BCP): An overview of the study design and protocol development. *Neuroimage, 185*, 891-905. doi:https://doi.org/10.1016/j.neuroimage.2018.03.049

Huppert, T. J., Franceschini, M. A., & Boas, D. A. (2009). Noninvasive Imaging of Cerebral Activation with Diffuse Optical Tomography. In R. D. Frostig (Ed.), *In Vivo Optical Imaging of Brain Function* (2nd ed.). Boca Raton, FL: CRC Press/Taylor & Francis.

Jacques, S. L., & Wang, L. (1995). Monte Carlo Modeling of Light Transport in Tissues. In A. J. Welch & M. J. C. Van Gemert (Eds.), *Optical-Thermal Response of Laser-Irradiated Tissue* (pp. 73-100). Boston, MA: Springer US.

Jenkinson, M., Pechaud, M., & Smith, S. M. (2005). BET2: MR-based estimation of brain, skull and scalp surfaces. *In Eleventh Annual Meeting of the Organization for Human Brain Mapping*.

Jernigan, T. L., Brown, T. T., Hagler, D. J., Akshoomoff, N., Bartsch, H., Newman, E., . . . Dale, A. M. (2016). The Pediatric Imaging, Neurocognition, and Genetics (PING) Data Repository. *Neuroimage, 124*, 1149-1154. doi:https://doi.org/10.1016/j.neuroimage.2015.04.057

Jurcak, V., Tsuzuki, D., & Dan, I. (2007). 10/20, 10/10, and 10/5 systems revisited: their validity as relative head-surface-based positioning systems. *Neuroimage, 34*(4), 1600-1611. doi:10.1016/j.neuroimage.2006.09.024

Kabdebon, C., Leroy, F., Simmonet, H., Perrot, M., Dubois, J., & Dehaene-Lambertz, G. (2014). Anatomical correlations of the international 10–20 sensor placement system in infants. *Neuroimage, 99*, 342-356. doi:https://doi.org/10.1016/j.neuroimage.2014.05.046

Koessler, L., Maillard, L., Benhadid, A., Vignal, J. P., Felblinger, J., Vespignani, H., & Braun, M. (2009). Automated cortical projection of EEG sensors: Anatomical correlation via the international 10–10 system. *Neuroimage, 46*(1), 64-72. doi:https://doi.org/10.1016/j.neuroimage.2009.02.006

Kumar Reddy, A. N., & Sagar, D. K. (2015). Half-width at half-maximum, full-width at half-maximum analysis for resolution of asymmetrically apodized optical systems with slit apertures. *Pramana, 84*(1), 117-126. doi:10.1007/s12043-014-0828-0

Li, G., Lin, W., Gilmore, J. H., & Shen, D. (2015). Spatial Patterns, Longitudinal Development, and Hemispheric Asymmetries of Cortical Thickness in Infants from Birth to 2 Years of Age. *The Journal of Neuroscience, 35*(24), 9150. doi:10.1523/JNEUROSCI.4107-14.2015

Li, G., Wang, L., Shi, F., Lyall, A. E., Lin, W., Gilmore, J. H., & Shen, D. (2014). Mapping Longitudinal Development of Local Cortical Gyrification in Infants from Birth to 2 Years of Age. *The Journal of Neuroscience, 34*(12), 4228. doi:10.1523/JNEUROSCI.3976-13.2014

Lloyd-Fox, S., Blasi, A., & Elwell, C. E. (2010). Illuminating the developing brain: The past, present and future of functional near infrared spectroscopy. *Neuroscience & Biobehavioral Reviews, 34*(3), 269-284. doi:https://doi.org/10.1016/j.neubiorev.2009.07.008

Lloyd-Fox, S., Richards, J. E., Blasi, A., Murphy, D. G., Elwell, C. E., & Johnson, M. H. (2014). Coregistering functional near-infrared spectroscopy with underlying cortical areas in infants. *Neurophotonics, 1*(2), 025006. doi:10.1117/1.NPh.1.2.025006

Lloyd-Fox, S., Wu, R., Richards, J. E., Elwell, C. E., & Johnson, M. H. (2013). Cortical Activation to Action Perception is Associated with Action Production Abilities in Young Infants. *Cerebral Cortex, 25*(2), 289-297. doi:10.1093/cercor/bht207

Makropoulos, A., Aljabar, P., Wright, R., Hüning, B., Merchant, N., Arichi, T., . . . Rueckert, D. (2016). Regional growth and atlasing of the developing human brain. *Neuroimage, 125*, 456-478. doi:https://doi.org/10.1016/j.neuroimage.2015.10.047

Mansouri, C., L'Huillier, J.-p., Kashou, N. H., & Humeau, A. (2010). Depth sensitivity analysis of functional near-infrared spectroscopy measurement using three-dimensional Monte Carlo modeling-based magnetic resonance imaging. *Lasers in Medical Science, 25*(3), 431-438. doi:http://dx.doi.org/10.1007/s10103-010-0754-4

Matsui, M., Homae, F., Tsuzuki, D., Watanabe, H., Katagiri, M., Uda, S., . . . Taga, G. (2014). Referential framework for transcranial anatomical correspondence for fNIRS based on manually traced sulci and gyri of an infant brain. *Neuroscience Research, 80*, 55-68. doi:https://doi.org/10.1016/j.neures.2014.01.003

Okamoto, M., Dan, H., Sakamoto, K., Takeo, K., Shimizu, K., Kohno, S., . . . Dan, I. (2004). Three-dimensional probabilistic anatomical cranio-cerebral correlation via the international 10–20 system oriented for transcranial functional brain mapping. *Neuroimage, 21*(1), 99-111. doi:https://doi.org/10.1016/j.neuroimage.2003.08.026

Okamoto, M., & Dan, I. (2005). Automated cortical projection of head-surface locations for transcranial functional brain mapping. *Neuroimage, 26*(1), 18-28. doi:https://doi.org/10.1016/j.neuroimage.2005.01.018

Perdue, K. L., Fang, Q., & Diamond, S. G. (2012). Quantitative assessment of diffuse optical tomography sensitivity to the cerebral cortex using a whole-head probe. *Physics in medicine and biology, 57*(10), 2857. doi:10.1088/0031-9155/57/10/2857

Perdue, K. L., Jensen, S. K. G., Kumar, S., Richards, J. E., Kakon, S. H., Haque, R., . . . Nelson, C. A. (2019). Using functional near-infrared spectroscopy to assess social information processing in poor urban Bangladeshi infants and toddlers. *Developmental Science, 22*(5). doi:10.1111/desc.12839

Perlman, S. B., Luna, B., Hein, T. C., & Huppert, T. J. (2014). fNIRS evidence of prefrontal regulation of frustration in early childhood. *Neuroimage, 85*, 326-334. doi:https://doi.org/10.1016/j.neuroimage.2013.04.057

Pinti, P., Tachtsidis, I., Hamilton, A., Hirsch, J., Aichelburg, C., Gilbert, S., & Burgess, P. W. (2020). The present and future use of functional near-infrared spectroscopy (fNIRS) for cognitive neuroscience. *Annals of the New York Academy of Sciences, 1464*(1), 5-29. doi:10.1111/nyas.13948

Powell, L. J., Deen, B., & Saxe, R. (2018). Using individual functional channels of interest to study cortical development with fNIRS. *Developmental Science, 21*(4), e12595. doi:10.1111/desc.12595

Raznahan, A., Shaw, P., Lalonde, F., Stockman, M., Wallace, G. L., Greenstein, D., . . . Giedd, J. N. (2011). How Does Your Cortex Grow? *The Journal of Neuroscience, 31*(19), 7174. doi:10.1523/JNEUROSCI.0054-11.2011

Remer, J., Croteau-Chonka, E., Dean, D. C., D'Arpino, S., Dirks, H., Whiley, D., & Deoni, S. C. L. (2017). Quantifying cortical development in typically developing toddlers and young children, 1–6 years of age. *Neuroimage, 153*, 246-261. doi:https://doi.org/10.1016/j.neuroimage.2017.04.010

Richards, J. E. (2013). Cortical sources of ERP in prosaccade and antisaccade eye movements using realistic source models. *Front Syst Neurosci, 7*, 27. doi:10.3389/fnsys.2013.00027

Richards, J. E. (in prep). Updating the Neurodevelopmental MRI Database.

Richards, J. E., Boswell, C., Stevens, M., & Vendemia, J. M. (2015). Evaluating methods for constructing average high-density electrode positions. *Brain Topogr, 28*(1), 70-86. doi:10.1007/s10548-014-0400-8

Richards, J. E., & Conte, S. (2020). Brain development in infants: Structure and experience. In C. Tamis-LeMonda & J. J. Lockman (Eds.), *Cambridge Handbook of Infant Development*. Cambridge: Cambridge.

Richards, J. E., Sanchez, C. E., Phillips-Meek, M. C., & Xie, W. (2015). A database of age-appropriate average MRI templates. *Neuroimage, 124*(Pt B), 1254-1259. doi:10.1016/j.neuroimage.2015.04.055

Richards, J. E., & Xie, W. (2015). Brains for all the ages: Structural neurodevelopment in infants and children from a life-span perspective. In J. Bensen (Ed.), *Advances in Child Development and Beahvior* (Vol. 48).

Rorden, C. (2012). MRIcroGL. *Retrieved from McCausland Center: http://www.mccauslandcenter.sc.edu/mricrogl/*.

Rorden, C., & Brett, M. (2000). Stereotaxic Display of Brain Lesions. *Behavioural Neurology, 12*, 421719. doi:10.1155/2000/421719

Sanchez, C. E., Richards, J. E., & Almli, C. R. (2012a). Age-Specific MRI Templates for Pediatric Neuroimaging. *Developmental Neuropsychology, 37*(5), 379-399. doi:10.1080/87565641.2012.688900

Sanchez, C. E., Richards, J. E., & Almli, C. R. (2012b). Neurodevelopmental MRI brain templates for children from 2 weeks to 4 years of age (vol 54, pg 77, 2012). *Developmental Psychobiology, 54*(4), 474-474. doi:10.1002/dev.21018

Schweiger, M., & Arridge, S. (2014). The Toast++ software suite for forward and inverse modeling in optical tomography. *Journal of Biomedical Optics, 19*(4), 040801.

Shattuck, D. W., Mirza, M., Adisetiyo, V., Hojatkashani, C., Salamon, G., Narr, K. L., . . . Toga, A. W. (2008). Construction of a 3D probabilistic atlas of human cortical structures. *Neuroimage, 39*(3), 1064-1080. doi:https://doi.org/10.1016/j.neuroimage.2007.09.031

Smith, S. M., Jenkinson, M., Woolrich, M. W., Beckmann, C. F., Behrens, T. E. J., Johansen-Berg, H., . . . Matthews, P. M. (2004). Advances in functional and structural MR image analysis and implementation as FSL. *Neuroimage, 23*, S208-S219. doi:https://doi.org/10.1016/j.neuroimage.2004.07.051

Strangman, G., Franceschini, M. A., & Boas, D. A. (2003). Factors affecting the accuracy of near-infrared spectroscopy concentration calculations for focal changes in oxygenation parameters. *Neuroimage, 18*(4), 865-879. doi:10.1016/s1053-8119(03)00021-1

Strangman, G., Li, Z., & Zhang, Q. (2013). Depth Sensitivity and Source-Detector Separations for Near Infrared Spectroscopy Based on the Colin27 Brain Template. *PLOS ONE, 8*(8), e66319. doi:10.1371/journal.pone.0066319

Strangman, G., Zhang, Q., & Li, Z. (2014). Scalp and skull influence on near infrared photon propagation in the Colin27 brain template. *Neuroimage, 85*, 136-149. doi:https://doi.org/10.1016/j.neuroimage.2013.04.090

Tran, A. P., Yan, S., & Fang, Q. (2020). Improving model-based functional near-infrared spectroscopy analysis using mesh-based anatomical and light-transport models. *Neurophotonics, 7*(1), 015008.

Tsuzuki, D., Cai, D.-s., Dan, H., Kyutoku, Y., Fujita, A., Watanabe, E., & Dan, I. (2012). Stable and convenient spatial registration of stand-alone NIRS data through anchor-based probabilistic registration. *Neuroscience Research, 72*(2), 163-171. doi:https://doi.org/10.1016/j.neures.2011.10.008

Tsuzuki, D., & Dan, I. (2014). Spatial registration for functional near-infrared spectroscopy: From channel position on the scalp to cortical location in individual and group analyses. *Neuroimage, 85*, 92-103. doi:https://doi.org/10.1016/j.neuroimage.2013.07.025

Tsuzuki, D., Homae, F., Taga, G., Watanabe, H., Matsui, M., & Dan, I. (2017). Macroanatomical Landmarks Featuring Junctions of Major Sulci and Fissures and Scalp Landmarks Based on the International 10–10 System for Analyzing Lateral Cortical Development of Infants. *Frontiers in Neuroscience, 11*(394). doi:10.3389/fnins.2017.00394

Tustison, N. J., Avants, B. B., Cook, P. A., Zheng, Y., Egan, A., Yushkevich, P. A., & Gee, J. C. (2010). N4ITK: Improved N3 Bias Correction. *IEEE Transactions on Medical Imaging, 29*(6), 1310-1320. doi:10.1109/tmi.2010.2046908

Wang, Ayaz, H., & Izzetoglu, M. (2019). Investigation of the source-detector separation in near infrared spectroscopy for healthy and clinical applications. *Journal of Biophotonics, 12*(11), e201900175. doi:10.1002/jbio.201900175

Wang, L., Jacques, S. L., & Zheng, L. (1995). MCML—Monte Carlo modeling of light transport in multi-layered tissues. *Computer Methods and Programs in Biomedicine, 47*(2), 131-146. doi:https://doi.org/10.1016/0169-2607(95)01640-F

Whiteman, A., Santosa, H., Chen, D., Perlman, S., & Huppert, T. (2017). Investigation of the sensitivity of functional near-infrared spectroscopy brain imaging to anatomical variations in 5- to 11-year-old children. *Neurophotonics, 5*(1), 011009.

Wijeakumar, S., Kumar, A., Delgado Reyes, L. M., Tiwari, M., & Spencer, J. P. (2019). Early adversity in rural India impacts the brain networks underlying visual working memory. *Developmental Science, 22*(5), e12822. doi:10.1111/desc.12822

Yan, S., Tran, A. P., & Fang, Q. (2019). Dual-grid mesh-based Monte Carlo algorithm for efficient photon transport simulations in complex three-dimensional media. *Journal of Biomedical Optics, 24*(2), 020503.

Yaroslavsky, A. N., Schulze, P. C., Yaroslavsky, I. V., Schober, R., Ulrich, F., & Schwarzmaier, H. J. (2002). Optical properties of selected native and coagulated human brain tissues in vitro in the visible and near infrared spectral range. *Phys Med Biol, 47*(12), 2059-2073.

Zhang, Y., Brady, M., & Smith, S. (2001). Segmentation of brain MR images through a hidden Markov random field model and the expectation-maximization algorithm. *IEEE Trans Med Imaging, 20*(1), 45-57. doi:10.1109/42.906424

Zimeo Morais, G. A., Balardin, J. B., & Sato, J. R. (2018). fNIRS Optodes' Location Decider (fOLD): a toolbox for probe arrangement guided by brain regions-of-interest. *Scientific Reports, 8*(1), 3341. doi:10.1038/s41598-018-21716-z

Supplemental Materials:

Table 1: Source-detector separation information for "all electrode pairs" constructed from 10-5 electrode locations.

It provides the minimum and maximum distances specified for each target separation distance (10mm to 60mm in 5mm increment) for all age groups.

Table 2: References of optical properties used in published studies.

Table 3: A looked-up table presenting the probabilistic mapping between scalp locations and atlas ROIs for all age groups.

The Scalp Projection method describes the anatomical correspondence between the 10-10 electrode locations and the atlas ROIs. The Source-Detector (S-D) Channel DOT method describes the sensitivity of the 10-10 channel positions to the atlas ROIs.

Table 4: A look-up table presenting the specificity of channels specified in the fOLD toolbox to the atlas ROIs for selected age groups (3-months, 6-months, and 20-24 years).

Figure 1: Mean numbers of nodes and elements for the dense and sparse finite element model (FEM) mesh by age group.

Figure 2: Mean numbers of source-detector channels selected for the target separation distances by age group.

Figure 3: Virtual channel placement for fOLD channels.

Figure 4: Mean S-D Channel DOT distances estimated with age-matched average templates separately by age group.

Figure 5: Mean scalp-to-cortex distances by sex and age groups. The distances were estimated with individual participant-based head models using Scalp Projection, Direct DOT, and S-D Channel DOT methods.

Figure 6: A comparison of Direct DOT and S-D Channel DOT distance measures from MCX and tMCimg outputs.

Figure 7. A comparison of S-D Channel DOT distance among estimation methods (MCX, MMC, and tMCimg) and head model types (individual head models and age-matched average templates) in 3- and 6-month-old infants.

Figure 8: A comparison of S-D Channel DOT distance among estimation methods (MCX, MCX with fOLD channels, MMC, and tMCimg) and head model types (individual head models and age-matched average templates) in 3- and 6-month-old infants.

Figure 9: Examples of S-D Channel DOT fluence sensitivity profile by channel from an individual subject in each age group at 20mm and 50mm separations.

Figure 10: Variance of S-D Channel DOT fluence sensitivity profile by age at 30mm and 50mm separations.